PL-TR-94-2146

AD-A285 845

RADAR STUDIES OF AVIATION HAZARDS

F. Ian Harris
Ralph J. Donaldson, Jr.
David J. Smalley
Shu - Lin Tung

Hughes STX Corporation
109 Massachusetts Avenue
Lexington, MA 02173

31 May, 1994

Scientific Report No. 1

APPROVED FOR PUBLIC RELEASE; DISTRIBUTION UNLIMITED.

PHILLIPS LABORATORY
Directorate of Geophysics
AIR FORCE MATERIEL COMMAND
HANSCOM AIR FORCE BASE, MA 01731-3010

"This technical report has been reviewed and is approved for publication."

PAUL R. DESROCHERS
Contract Manager

DONALD A. CHISHOLM
Chief, Satellite Analysis and Weather
Prediction Branch
Atmospheric Sciences Division

DONALD A. CHISHOLM, Acting Director
Atmospheric Sciences Division

This report has been reviewed by the ESC Public Affairs Office (PA) and is releasable to the National Technical Information Service (NTIS).

Qualified requestors may obtain additional copies from the Defense Technical Information Center (DTIC). All others should apply to the National Technical Information Service (NTIS).

If your address has changed, or if you wish to be removed from the mailing list, or if the addressee is no longer employed by your organization, please notify PL/TSI, 29 Randolph Road, Hanscom AFB, MA 01731-3010. This will assist us in maintaining a current mailing list.

Do not return copies of this report unless contractual obligations or notices on a specific document requires that it be returned.

REPORT DOCUMENTATION PAGE

Form Approved
OMB No. 0704-0188

1. AGENCY USE ONLY (Leave blank)	2. REPORT DATE	3. REPORT TYPE AND DATES COVERED
	31 May, 1994	Scientific Report No. 1

4. TITLE AND SUBTITLE

RADAR STUDIES OF AVIATION HAZARDS

5. FUNDING NUMBERS

F19628-93-C-0054
PE63707F
PR2781
TAGT
WUMA

6. AUTHOR(S)

F. Ian Harris, Ralph J. Donaldson, Jr.,
David J. Smalley and Shu-Lin Tung

7. PERFORMING ORGANIZATION NAME(S) AND ADDRESS(ES)

Hughes STX Corporation
109 Massachusetts Avenue
Lexington, MA 02173

8. PERFORMING ORGANIZATION REPORT NUMBER

Hughes STX Scientific Report #2

9. SPONSORING / MONITORING AGENCY NAME(S) AND ADDRESS(ES)

Phillips Laboratory
29 Randolph Road
Hanscom AFB, MA 01731-3010

Contract Manager: Paul R. Desrochers/GPAB

10. SPONSORING / MONITORING AGENCY REPORT NUMBER

PL-TR-94-2146

11. SUPPLEMENTARY NOTES

12a. DISTRIBUTION / AVAILABILITY STATEMENT

Approved for public release; distribution unlimited

12b. DISTRIBUTION CODE

13. ABSTRACT *(Maximum 200 words)*

During the first year of this contract, research was directed toward the development of new techniques to monitor and forecast weather related aviation hazards with Doppler weather radar. Focus was on the characterization of the structure of severe convective storms and of synoptic scale baroclinic fronts. One aspect that was examined is the detection and quantization of the weak echo region usually seen in severe convective storms. Another has been the search for lightning precursors. Finally, considerable effort has been expended on the automated depiction of the wind and precipitation structure associated with baroclinic fronts.

14. SUBJECT TERMS	15. NUMBER OF PAGES
Doppler weather radar, automated techniques, front detection, gradient computation, severe storm structure, lightning precursors	94
	16. PRICE CODE

17. SECURITY CLASSIFICATION OF REPORT	18. SECURITY CLASSIFICATION OF THIS PAGE	19. SECURITY CLASSIFICATION OF ABSTRACT	20. LIMITATION OF ABSTRACT
Unclassified	Unclassified	Unclassified	Unlimited

TABLE OF CONTENTS

LIST OF FIGURES

LIST OF TABLES

RADAR STUDIES OF AVIATION HAZARDS

1. INTRODUCTION

This is the first annual report being presented by Hughes STX Corporation upon completion of the first year of a total of three years under Contract No. F19628-93-C-0054. This report presents a summary of the research conducted during the past year and a brief presentation of plans for the upcoming year. The goal of this contract is for Hughes STX to develop and test algorithms/techniques that will be candidates for inclusion in the NEXRAD algorithm inventory. Phenomena of particular interest to the Air Force are being addressed: precursors to severe weather (tornadoes, hail, severe wind events), precursors to lightning development, and monitoring of potentially hazardous weather and wind associated with baroclinic front situations. Efforts in each of these three areas will be described in turn.

2. SEVERE STORM STRUCTURE

2.1. Introduction

Hail, damaging winds, tornadoes, heavy rain, and flash flooding have long been associated with thunderstorms. Since World War II, probing by radar has led to many important discoveries concerning the structure of severe thunderstorms. Recently, Doppler weather radar has become the paramount source of data for meteorological researchers to use to further the understanding of these phenomena. It has helped to advance our understanding of thunderstorm structure and life cycle to the realization that a small subset of all thunderstorms, the supercells, account for a disproportionately high percentage of all thunderstorm-related mayhem.

Browning and Ludlam (1962) and Donaldson (1962), using conventional radars, were the first to report on the salient features of supercells; particularly the reflectivity echo hole associated with a strong, organized updraft. Armstrong and Donaldson (1969), using Doppler radar, discovered evidence of a cyclonic vortex within a severe thunderstorm collocated at times with the updraft region. Today this vortex is commonly called a mesocyclone and the echo hole has been termed by Chisholm (1973) the Weak Echo Region (WER) or, if bounded completely by high reflectivity, the Bounded Weak Echo Region (BWER).

The purpose of this section is to detail the progress made in the development of a Severe Storm Structure algorithm. The initial phase of this task involved the selection of candidate severe storm structure features based on current knowledge that could lend themselves to such an algorithm. This section documents the techniques developed to help identify some of these structures as observed in the reflectivity field for individual elevation scans. The overall goal of the algorithm is to quantify these identified structures so as to assess the potential for and intensity of severe weather.

The section is separated into a number of sub-sections beginning with one (2.2) on the important advancements in the understanding of thunderstorms prior to the designation of supercells as a special type. Sub-section 2.3 is on supercells. This includes discussion of its distinguishing features, life cycle, and variations in form particularly as viewed in the reflectivity. Sub-section 2.4 provides a discussion of the potential of some supercell features for use in a structure algorithm. This leads into the discussion, in sub-section 2.5, of the current identification techniques developed for the beginnings of the Severe Storm Structure algorithm. Emphasis is placed on the development of BWER identification techniques and the utility of these techniques in the identification of other features (e.g., WER).

2.2. Early Research Into Thunderstorms

Prior to the identification of supercells, the study of thunderstorms led to the discovery of important clues into the true nature of severe storms. Byers and

Braham (1949), from the Thunderstorm Project, were the first to provide a concise description of the life cycle of a single-cell thunderstorm. A cell in this context is considered to be the convection cell of a cumulonimbus cloud characterized by a couplet of upward and downward motion. This simple thunderstorm evolves through three stages in its one hour life cycle. In the development stage, an updraft initiates a cumulus cloud that grows into a cumulonimbus cloud. The mature stage is reached when the precipitation falls back through the generating updraft. The resulting downdraft overwhelms the updraft in the final stage of the storm. This typical storm travels with the mean, mid-level, environmental wind and rarely produces weather more severe than a moderate gust front.

Most thunderstorms do not have the simple structure and evolution as described above. In fact, Burgess and Lemon (1990) note that multicellular thunderstorms are the most common type to occur in North America. Convergence created by gust fronts or orographic features often results in the production of a succession of single cells that merge or interact to form multicellular thunderstorms. Under certain conditions, a single cell or multicellular thunderstorm evolves into a thunderstorm with somewhat unicellular characteristics that appear quasi-steady-state for a few hours. These storms usually produce extremely severe weather and are known as supercells.

The focus of the research community shifted to severe thunderstorms after Byers and Braham published their single cell description. Donaldson (1990) has reviewed the advances that have been made. Many severe storm features were uncovered. Donaldson *et al.* (1960) noted the positive correlation between the height of the thunderstorm echo top with respect to the tropopause and thunderstorm severity in New England. Donaldson (1961) also reported that the magnitude and altitude of the peak reflectivity of the core in a storm were positively correlated with thunderstorm severity. Both of these findings indicate that thunderstorm severity appears to be correlated with intense, deep convection.

2.3. Supercell Research

2.3.1. Distinguishing Features

Browning and Ludlam (1962) reported on the observed characteristics of a severe hailstorm in Wokingharn, England. This first reported supercell exhibited an echo-free vault beneath a nigh reflectivity core aloft. Donaldson (1962) reported that an Oklahoma storm had strikingly similar features, in this case calling the vault a chimney. Browning and Donaldson (1963) formally compared the two storms noting that they shared important characteristics. The authors surmised that the radar observable reflectivity features of these supercells were indicative of an exceptionally persistent, powerful, and organized updraft. This vigorous updraft is the distinguishing characteristic of a supercell and functions as its catalyst.

A number of features were common to both supercells. The echo-free vault is due to droplets being swept high into the storm by the strong updraft before they reach a highly reflective size. A high reflectivity core observed above the vault is due to droplet growth and vertical convergence in the decelerating updraft. A mid-level echo overhang results from the interaction between the divergent flow above the maximum vertical velocity and the environmental winds. The wall of reflectivity about the vault is from the curtain of precipitation descending outside the updraft. The overall reflectivity pattern often appears to be somewhat steady-state. A hook or pendant shape to the right-rear of the low-level weak echo region was also noted.

Chisholm (1973) studied 29 hailstorms in Alberta, Canada. He reported on some of the storms that exhibited vaults. Because of the vault's appearance on a Plan Position Indicator (PPI) radar scope, he named this feature the Bounded Weak Echo Region (BWER) or, if high reflectivity did not completely surround the weak echo, the Weak Echo Region (WER). These acronyms are now used to denote these features in radar meteorology. In his study, Chisholm devised the Loaded Moist Adiabatic model based on parcel theory to estimate the vertical velocity structure of the updraft and cloud parameters of the observed storms. Basically, the model assumed steady-state conditions with no entrainment and with condensed water carried in a one-dimensional updraft. Sounding data were used to initiate the

model. He calculated storm echo top from the model and compared it to that observed for the 29 storms and found agreement within 0.8 km for 75% of the cases. Considering this, he separated the storms into low, medium, and high energy groups. From this he found that the greater the energy available to a storm, the greater the maximum vertical velocity, storm top, and surface-observed hailstone size. The combination of observations and results from the simple model further the notion that storm severity was related to the storm's ability to develop deep into the atmosphere.

Another fundamental feature of the supercell was revealed by Doppler radar since it provides the means to monitor the radial component of the velocity in addition to reflectivity. Armstrong and Donaldson (1969) used a Plan Shear Indicator (PSI) for visual display of the tangential shear of the observed radial velocities. This shear was suspected to be caused by a vortex. During severe thunderstorms, they observed that indication of a PSI cyclonic vortex signature was related to the occurrence of damaging winds and hail. Significantly, it was noticed that, at times, this signature was incomplete (i.e., as if partially erased) due to the lack of signal within the weak echo area. This suggested a temporary collocation of the cyclonic vortex with a BWER. Donaldson (1970) concisely describes the process of vortex identification with Doppler radar radial velocity signatures. Greater confidence is allowed if the vortex signature has a vertical extent at least that of its horizontal diameter. This cyclonic vortex is commonly referred to as the mesocyclone. The mesocyclone generally forms at mid-levels with or near the updraft. It is indicative of vorticity within the supercell. As it evolves, the mesocyclone expands vertically up into and down through the storm. The interaction of the mesocyclone with other processes within the supercell and its relationship to severe weather are extensively reported on in the literature and are beyond the scope of this report.

Many others have since summarized their observations of the supercell structure, favorable environment/initiation modes, and life cycle (Weisman and Klemp, 1986; Rotunno, 1986; Burgess and Lemon, 1990; Ray, 1990; Lemon and Doswell, 1979). Their findings consistently identified specific traits to be associated

with supercells and corroborate those from earlier studies. Observations of the following traits are considered sufficient to identify a thunderstorm as a supercell

- long life that can last upwards of six hours,
- quasi-steady-state appearance,
- motion to the right of the mean mid-level environmental wind,
- a mesocyclone (rotating updraft) observed in the velocity field,
- a BWER (or WER) at mid-levels in a region of very high reflectivity marked by strong reflectivity gradients, capped by a high reflectivity core aloft, and associated with the maximum echo top,
- a mid-level echo overhang extending above and beyond a low-level WER at the right-rear flank. The WER is marked by strong reflectivity gradients,
- very strong, precipitation-laden downdraft and resultant gust front, and
- frequently a low-level hook-shaped echo.

2.3.2. Life Cycle

The life cycle of a supercell has three stages: growth (i.e., development), maturity, and collapse (i.e., decay) stages. This life cycle occurs over a period of many hours. Supercell development is typically preceded by multicellular thunderstorms (Lemon, 1977) for which individual cells, generally on the south flank, successively develop into increasingly stronger cells. Single cell thunderstorms also can develop into supercells. After about an hour one of the cells, often the strongest within a multicellular thunderstorm, suddenly grows rapidly and begins to move to the right of the environmental wind of the storm (cloud mass) layer. Also about this time, a low-level WER develops in response to the strengthening updraft along with an overhang and mesocyclone at mid-levels. The exact altitude implied by the term "mid-level" actually encompasses a range dependent on seasonal and latitudinal variations of the atmosphere. For instance, the overhang feature is depicted in

vertical cross-sections by Weisman and Klemp (1986) at about 6 km AGL for a midwestern storm while Chisholm (1973) shows this feature at about 4 km for an Alberta hailstorm. Thus, low- and high-level designations imply a relative altitude region below or above, respectively, the height of the mid-level features.

The mature stage typically is reached in about ninety minutes. At this time, the mesocyclone builds downward, the downdraft intensifies, and a BWER develops at mid-levels in response to the even stronger updraft. Weak tornadoes have been observed during this stage. Essentially the BWER is bounded since it has extended significantly into the mid-level echo overhang. In cross-section, the BWER is depicted with about 3-5 km of vertical extent. During collapse (or decay), the BWER fills with precipitation as the echo top descends. The areal size of the mid-level echo overhang decreases. The downdraft reaches a peak resulting in the very strong gust front. This is the time of major tornado occurrence. The storm eventually dissipates.

2.3.3. Favorable Environment

Two necessary ingredients for development of supercells are the availability of low-level moisture and favorable vertical distributions of wind shear in the atmosphere. The environmental hodograph is typically used to depict the characteristics of wind in the atmosphere. In a modeling exercise, Brooks and Wilhelmson (1993) note that greater hodograph curvature (and implied shear vector turning) resulted in greater updraft velocities. Brown (1990, 1993) notes that many composite hodographs portraying the pre-supercell environment are based on constant altitude or pressure-level averaging. Thus, features at non-standard levels are overlooked. He developed a technique in which pre-supercell hodograph features are considered relative to each other. This technique incorporates the construction of a composite hodograph that essentially maintains these structural features and depicts the mean layer thickness between them. This development led to a refinement of the usual pre-supercell environmental hodograph. With this refined hodograph, Brown showed that an environment favorable for supercell development has strong directional shear in the lowest 3 km capped by a 3 km layer of minimal shear. This latter feature could not be seen in the constant level analysis method. Topping this is a deep layer of strong speed shear up to the tropopause.

Doppler radar analyses depict the mesocyclone initiated at mid-levels, followed by growth in vertical extent as the supercell reaches maturity. In his dual-Doppler analysis of a supercell, Brown (1992) detected updraft rotation that was initiated through vorticity generated from couplets. These couplets were created by the blocking of mid-level environmental winds by the first, non-rotating updraft. It is particularly noteworthy that there was not one persistent updraft but a succession of distinct updrafts seen in the analysis. The second updraft flowed up into the cyclonic couplet at mid-levels created through blocking by the first updraft and, thus, gained rotation. Each successive updraft did likewise. Additionally, the storm's echo top seemed to vary in height in response to this updraft scenario. During this succession of updrafts, the lower-level reflectivity appears somewhat steady-state. This is because of the combined effects of the dynamical, microphysical, and environmental processes in the storm. Browning and Donaldson (1963), among others, report on the rise and fall sequence of the echo top (and echo core) in response to updraft evolution. From Brown's observations of the Agawam, OK storm, one might surmise that echo top variability during a storm may be due to successive updrafts as opposed to changes (or pulses) within one persistent updraft. It is not obvious if discrete updraft succession or pulses within one updraft will complicate identifying and quantifying BWERs or WERs within a supercell based exclusively on reflectivity data.

2.3.4. Low-Precipitation and High-Precipitation Supercells

Some researchers have grouped supercells into subclasses as observations indicate a natural variability among these storms. Supercells now are generally considered classic (as described previously), low-precipitation (LP), or high-precipitation (HP). The basic, distinctive features of the classic supercell are also found in the LP and HP types. It is important, however, to examine how their radar reflectivity characteristics differ by type. Sometimes classification appears justified but Bluestein and Parks (1983) and Moller *et al.* (1990) note that in other instances these subclasses may simply represent phases of the overall supercell evolutionary process.

Visual accounts by spotters led to the initial class distinctions of supercells. The LP supercell is characterized by a lack of noticeable precipitation below cloud base (Bluestein and Parks, 1983) that enables a clearer view of features sometimes obscured in classic storms. These LP supercells have been characterized as skeletons of the classic supercell (Bluestein and Woodall, 1990). HP storms, conversely, tend to have important features obscured by precipitation. Spotters report difficulty in identifying severe weather features like hail and tornadoes due to precipitation shrouding.

Beyond the surface-observable visual differences of these supercells, radar reflectivity observations have shown that LP supercells can have modified radar signatures compared to the classic supercell. Bluestein and Parks (1983) found LP storms typically formed along or near drylines in an environment with reduced low-level moisture and weaker shear than that for classic supercells. While these storms lacks precipitation and strong surface downdrafts, they still produced tornadoes and large hail. Bluestein and Woodall (1990) note that, in Doppler radar data, the LP storm appears unicellular. Its updraft tends to be small and rotating, but only 2-3 km in the horizontal, which is smaller than usual. These storms typically drop a narrow swath of large hail. This hail is the cause of the high reflectivity core aloft.

HP supercells are less likely to produce strong or violent tornadoes than the classic type but have yielded unusually long, wide, and destructive hail swaths (Nelson, 1987). They have also produced flash flooding and prolonged downburst events. The HP supercell preferentially forms along pre-existing boundaries such as old outflow lines or stationary fronts, but not drylines. They also have been triggered in association with upper-level short wave troughs. Mecikalski and Evenson (1993) studied supercells in the Great Lakes region. They found that supercells tended to be of the HP type and produced few tornadoes. The authors conclude that, for the Great Lakes region, it may be important to monitor environmental conditions to assess the potential for HP development when forecasting severe weather.

The HP supercell may be the most convoluted and evolutionary of the three supercell types. These storms have been described as hybrid or multicellular/ supercellular in form (Weaver and Nelson, 1982). Observations indicate these

storms could have multiple BWERs with strong mesocyclones or a large BWER concurrently fed by multiple updrafts (Nelson, 1987). Of interest, is that HPs often transform into a bow echo (BE) form. This transformation can be very fast. Comma-shape echoes are also commonly observed with these storms. These echo features are in response to the complex interactions of multiple circulations influencing the storm. The comma-shape echo is associated with the migration of the mesocyclone from the forward center to the left rear flank in the mature stage of the HP supercell. It is at this time that there is the greatest chance of severe weather. The bow echo evolves in the decaying stage as the comma head broadens or in an intermediate phase when multiple circulations exit in various stages of development. Sometimes the bow echo form is averted because the associated mesocyclone travels north and east with a resultant comma-shape echo (Morse *et al.*, 1993).

From these various HP scenarios a plethora of radar reflectivity signatures have been described beyond the typical BWER distinction. They are modified from the classic sense and have the potential to be mired in confusion in BE or multicellular situations. Distinctions of importance are that the low-level WER is located on the east-central section of the echo (as opposed to the right rear location) and, due to multiple updrafts, it is broader in area. This resultant shape has been likened to a kidney bean (right side concavity). The HP supercell reflectivity signature is usually spatially larger than that of classic supercells with persistently higher reflectivity (50+ dBZ) aloft. Additionally, an S-shape pattern results from a notching of the reflectivity in response to drier mid-level, rear inflow (called the RIN-rear inflow notch). The appearance of this S-shape (most pronounced at low levels) has been associated with the onset of HP severe weather and the comma-shape feature (Pryzbylinski *et al.*, 1993). It may be that the significant addition of dry air at mid-levels (as the RIN indicates) provides the source for enhanced evaporation causing intensification of the downdraft.

HP supercells have been further separated into cool and warm season varieties. Cool season HPs tend to form within squall lines while warm season HPs are more apt to be isolated. A unique feature of warm season HPs is a large, high reflectivity (35-45 dBZ) area below 2 km near the right rear flank of the primary

reflectivity core. The 50+ dBZ core extends about twice as high (8-10 km) in the warm season as in the cool. This seems likely to be a direct response to seasonal thermal differences in the atmosphere. For both warm and cool season HP supercells, multiple BWERS and mesocyclones are observed. At times, multiple occurrences of each feature exist simultaneously. In either season, the first BWER and mesocyclone are the most long-lived (on average, 30 and 45 minutes, respectively). Subsequent BWERs and mesocyclones last, on average, 10 and 30 minutes, respectively.

2.4. Algorithm Considerations

The above discussion provides the basis for the nomination of candidate features for supercell identification and quantification. Strong associations have been identified between the size and intensity of the updraft and the occurrence of severe weather. We suspect that the size of the BWER and its reflectivity deficit are linked to the updraft's characteristics. It is not possible to use a single Doppler radar to directly evaluate the updraft. Candidate radar reflectivity features should be examined for suitability for inference of updraft strength. Besides citing the storm echo top and peak reflectivity as parameters related to updraft strength, Lemon (1977) stresses the importance of the BWER and WER, updraft tilt, and the echo overhang. Candidate features would obviously include:

- the BWER,
- the WER,
- reflectivity core aloft,
- updraft tilt,
- mid-level echo overhang, and
- echo top evolution.

It is likely that some combination of these and possibly other features will lead to a set of quantified information to correlate to severe weather. A logical approach is to identify the appropriate features in an elevation scan and, then, build and quantify the features into three dimensions. The techniques used should take advantage of the unique structural features of the supercell especially suited for such

a task. Ideally, the techniques adopted would also be suitable for more than one structural feature (e.g., functional for both the BWER and WER).

The distinction of HP and LP supercells as separate from the classic supercell raises many microphysical and dynamical questions. Whether they truly represent either discrete subclasses or stages in a supercell's evolutionary process, the reflectivity signature modifications associated with these supercells complicate the ability for an algorithm to be all encompassing as it first tries to identify and, then, quantify the feature. The broad flatness of the HP WER and the smallness of the LP, in general, pose difficult limiting cases for a structure identification algorithm.

2.5. Techniques

The goal of the Severe Storm Structure algorithm is to identify and quantify structural characteristics associated with supercells and to relate those characteristics to the occurrence of severe weather. This algorithm must be computationally conservative to allow real-time implementation. Initially, identification and quantification of the BWER will be the focus of attention. The BWER has been selected because of its distinctive structure and strong association with an intense updraft. For the near term, the identification process will be restricted to reflectivity field considerations. The remainder of this report is dedicated to a discussion of the techniques examined for BWER identification.

To the knowledgeable radar operator, a distinct BWER is readily identified in a PPI display. In plan view, this feature consists of a ring (or ridge) of high reflectivity surrounding a distinct minimum. Outside this ring, the reflectivity decreases. Thus, a transit through the feature reveals an alternating pattern of reflectivity magnitude trends. The reflectivity magnitudes in this ring are usually amongst the highest within the observational plane. This reflectivity ridge will be used to define the boundary for the BWER. The identification problem, therefore, reduces to the extraction of signatures related to these BWER reflectivity characteristics.

The identification task involves the development of a technique to locate the reflectivity ridge. This technique must be able to treat complex structures such as variable reflectivity values along the ridge, multiple HP BWERs, and weak reflectivity

areas within or between storms. Resolution issues must also be considered. Lemon (1977) notes that BWERs generally have horizontal dimensions less than or equal to 8 km. Therefore, there could be performance degeneration with range which needs to be assessed. In addition, the effects of sidelobe contamination, especially within the BWER, must be considered.

Characteristics of the BWER can be quantified upon successful identification of the BWER ridge outline. Quantities to be calculated might include an estimation of the reflectivity deficit in the WER and its implied water deficit. Reflectivity deficit is defined as the amount of reflectivity necessary to fill the BWER to reflectivity values equivalent to those on the ridge. The water deficit would be the water mass equivalent for such a deficit. For these deficit computations, the variability of the reflectivity magnitude along the ridge will need to be considered. A measure of this variability could also be useful in determining the bounded nature of the WER. Shape parameters such as major and minor axes should be examined. Questions to be addressed include: Is a large BWER with a minor deficit more indicative of updraft strength than a small BWER with a large deficit? What spatial values define "large", "small", and "minor" in this situation? It is expected that these issues will be resolved via analysis of many BWERs.

As stated earlier, the algorithm is intended for real-time operation and must be computationally conservative. Our goal is to develop techniques to identify the BWER based on the reflectivity field characteristics used for visual identification. For these reasons, it was decided to develop techniques that process the data independent of their spherical coordinates and that utilize pattern recognition concepts. Upon identification of the BWER ridge, cell positions would be considered in spherical coordinates for use in quantification efforts. To assist in the ridge identification, a "machine intelligent" approach is examined. Delanoy and Troxel (1993) used such a technique with impressive results for the detection of gust fronts in central Florida.

2.5.1. Reflectivity Data Preprocessing

Pattern vectors are constructed from a B-scan array of reflectivity data analogous to those created from radial velocity data. A B-scan is a two-dimensional

array of radar data arranged gates by radials. A pattern vector is a line constructed along a radial or constant-range arc in which all data points between the first and last have a data gradient of the same sign. To reduce the computational load, pattern vectors were constructed only for that portion of the supercell thought to have the greatest likelihood of a BWER. This region is determined by focusing on the region of highest reflectivity. To do this, each radial is processed to yield an average of its top 30% reflective gates. An overall mean overall beams of these averages is then computed. Maximum and minimum azimuth bounds are then determined by accepting any radial that has at least three range gates exceeding this overall mean reflectivity. All data within these bounds are then processed even if some radials failed to meet the original criteria.

This simple method has proved to be very effective for the limited data examined to date. However, some modifications may be necessary as experience is gained. An obvious modification would be to restrict data processing in range as well as azimuth. This would essentially result in a boxed region of high reflectivity within an overall storm. Another concern is the treatment of multiple storms in a full scan. As currently configured, this method will only be successful for single storms. Therefore, for a more general scheme it will be necessary to identify boundaries of all storms in a scan. The current Storm Series set of NEXRAD algorithms (Klazura and Imy, 1993), perhaps with modifications introduced by Witt and Johnson (1993), may provide the means of computing these boundaries. We will continue to examine this problem.

The other preprocessing step involves the handling of outliers. A 25 cell window (5 range gates by 5 radials) is applied across the entire storm region prior to the high reflectivity bounding sequence. The standard deviation and mean of the 25 cells are computed. Any cell whose value falls outside a 2.5 standard deviation (s.d.) limit is replaced with the mean computed from an 8-neighbor mask. It was found that 2 s.d. was too strict a criterion while 3 s.d. was too lenient. Occasionally, a very small s.d. computed in regions of weak reflectivity gradient results in one or two cells being unnecessarily replaced. However, the impact of these unnecessary replacements is very small compared to the improvement derived from the

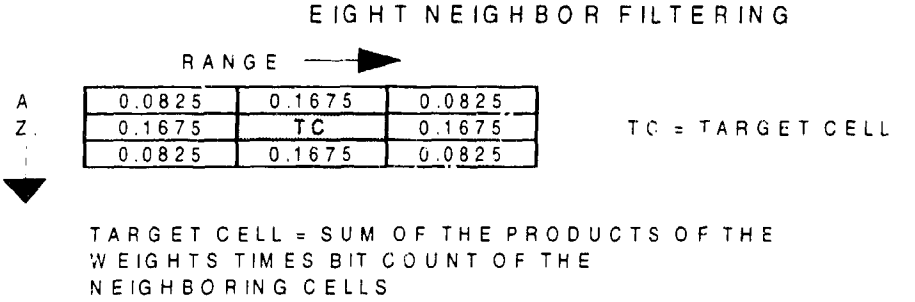

Figure 1. The averaging filter applied to a target cell.

elimination of the outliers. The 8-neighbor filter used to replace outliers is illustrated in Figure 1.

2.5.2. Pattern Vectors

With the elimination of outliers and the identification of the high reflectivity processing region, the reduced B-scan array is ready for pattern vector (PV) processing. The reflectivity data are processed as bit counts, the form of the output from the Doppler processor. These bit count data are range normalized and are proportional to reflectivity factor (dBZ). Positive and negative reflectivity gradient PVs are constructed. They are processed cross-range (along a radial) and cross-azimuth (at a constant range). From a pattern recognition perspective, the bit count value of each cell is a measure of intensity. Figure 2a shows a section of reflectivity bit count data. Figure 2b shows the cross-range PVs while Figure 2c depicts the cross-azimuth PVs associated with Figure 2a. For example, a positive reflectivity gradient PV in the cross-range direction defines a region along a radial in which reflectivity differences between cells are positive or zero. The PV is terminated when it encounters a cell difference of opposite sign. Cross-azimuth PVs are computed in a clockwise sense while cross-range ones are computed outward along a radial. A minimum of two links (3 adjacent cells) of the same trend is required for PV acceptance. This eliminated most inconsequential gradients. Note that as distance

from the radar increases, the true minimum distance for a cross-azimuth pattern vector also increases.

After positive and negative reflectivity gradient PVs of cross-range and cross-azimuth type are constructed, extrema are identified. Figure 3 illustrates the locations of extrema based on the sample data of Figure 2. These extrema are found where the start (end) cell of a PV is coincident with the end (start) cell of an opposite signed PV. Cross-range and cross-azimuth PV computations and pairings are independent. These extrema, in fact, are local maxima or minima in the reflectivity domain. It is likely, but not guaranteed, that a majority of the extrema detected along the BWER ridge outline correspond to maximum reflectivity bit count values for the individual cross-range or cross-azimuth processing passes. It is possible for a particular cell to be assigned extremum status from both types. A cell that is designated as an extremum represents a minimum of 5 consecutive cells. Its construction requires, as a minimum, a positive PV involving three cells, a negative PV involving three cells, and a common extremum cell.

Sample Reflectivity Bit Count

AZIMUTH \ RANGE (KM)	50.1	50.4	50.7	51.0	51.3	51.6	51.9	52.2
310.08	169	177	181	195	190	180	173	180
310.69	177	190	196	211	202	184	179	181
311.31	192	198	211	218	202	185	189	189
311.84	203	208	224	216	193	191	196	200
312.36	204	218	231	213	194	195	204	210
312.89	206	224	227	210	202	201	217	229
313.51	210	220	225	210	204	212	232	244
314.12	211	219	221	212	206	220	241	256
314.65	214	221	219	209	213	229	248	263
315.26	219	218	217	215	220	236	252	260
315.79	223	218	216	222	224	235	251	257
316.41	227	228	225	218	224	237	252	257
317.02	231	237	225	222	225	245	257	265
317.55	233	241	234	225	229	248	254	275

(a)

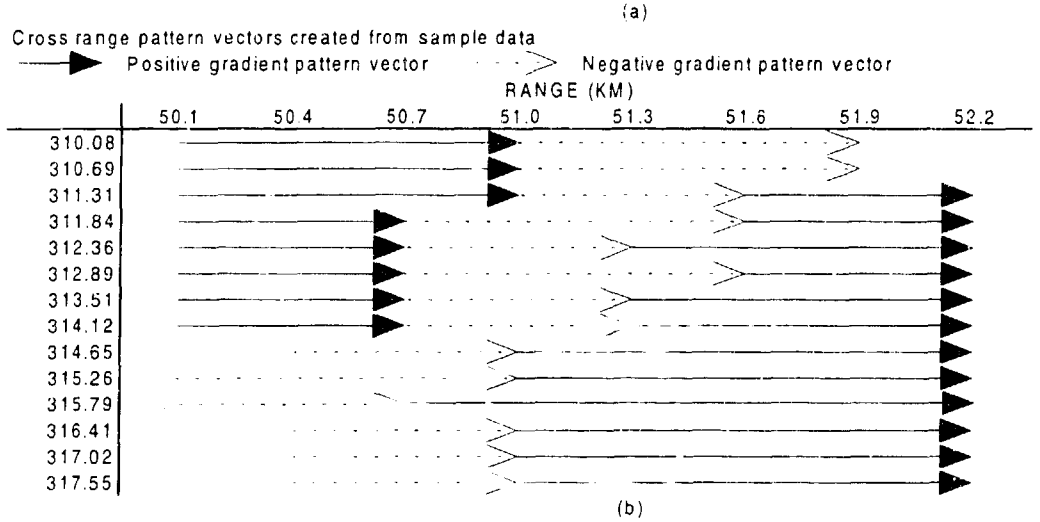

(b)

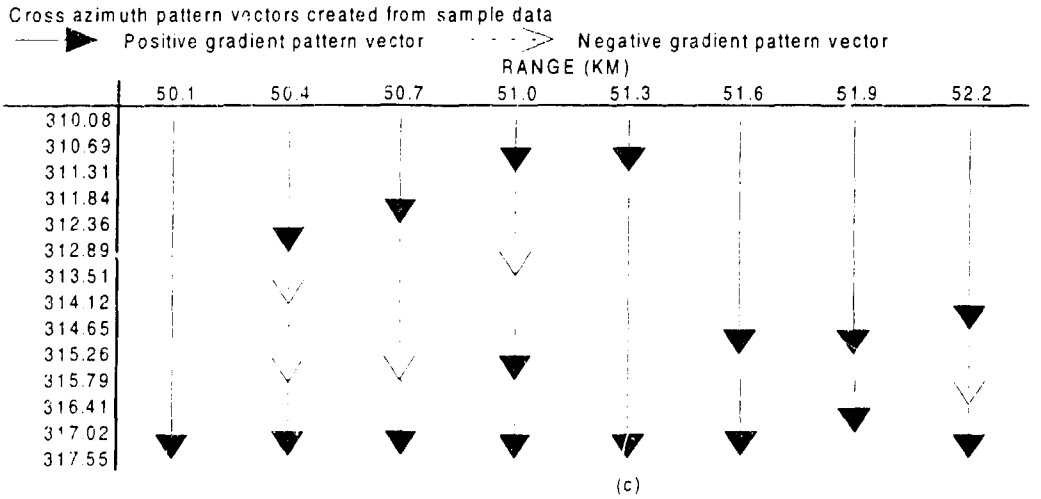

(c)

Figure 2. A sample B-scan of bit count reflectivity data are shown in (a). Cross-range (b) and cross-azimuth (c) pattern vectors based on this B-scan are also indicated. See text for discussion of pattern vectors.

2.5.3. Model and Control BWER Data

Two arrays of reflectivity data are used to gain an understanding of the role of extrema in the BWER identification process. One is for a Model BWER that consists of a reflectivity minimum surrounded by a ring of high reflectivity. There are no spurious data to be filtered. Figure 4 provides a three-dimensional (3D) representation of this model. The second array, the Control BWER, consists of data for the 5° elevation scan at 1803 CST of the Piedmont, OK storm of April 30, 1978. Figure 5 is a 3D depiction of these data. These 3D representations are useful to give a sense of the reflectivity gradients inherent in the data. A subjective analysis of the Control BWER data was performed to use as a reference for the assessment of techniques being applied in this study.

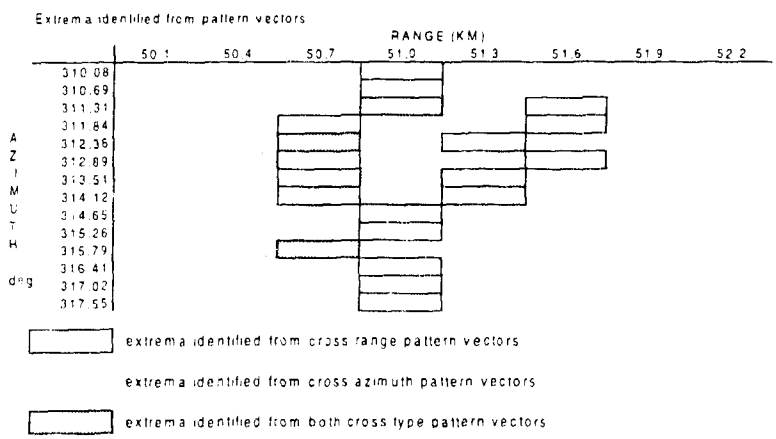

Figure 3. Extrema identified through the pattern vector process described in the text for the sample from Figure 2.

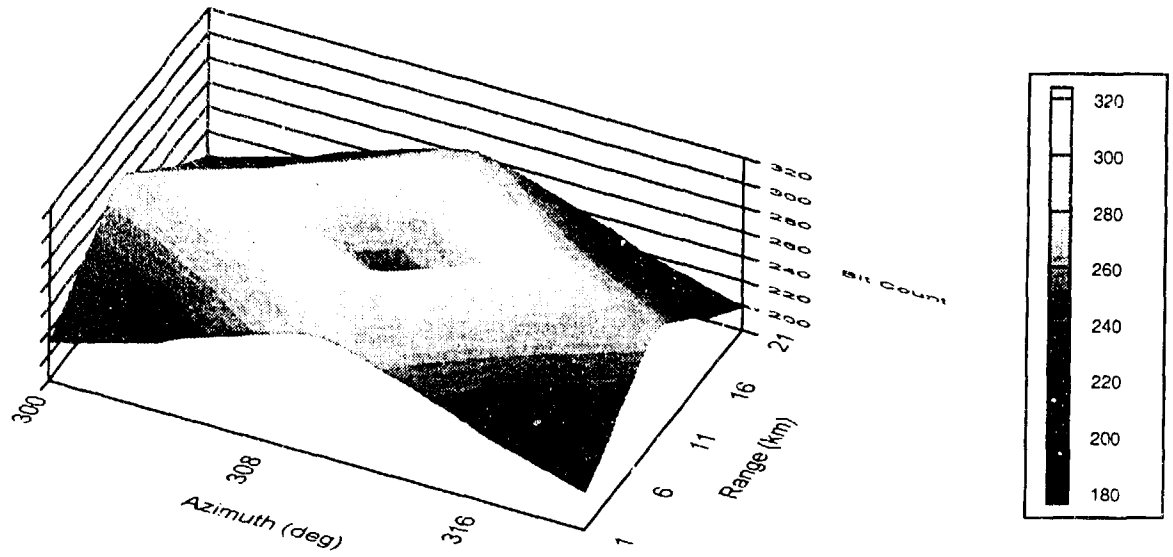

Figure 4. Three dimensional representation of the Model BWER. The BWER is centered about 10 km and 310°.

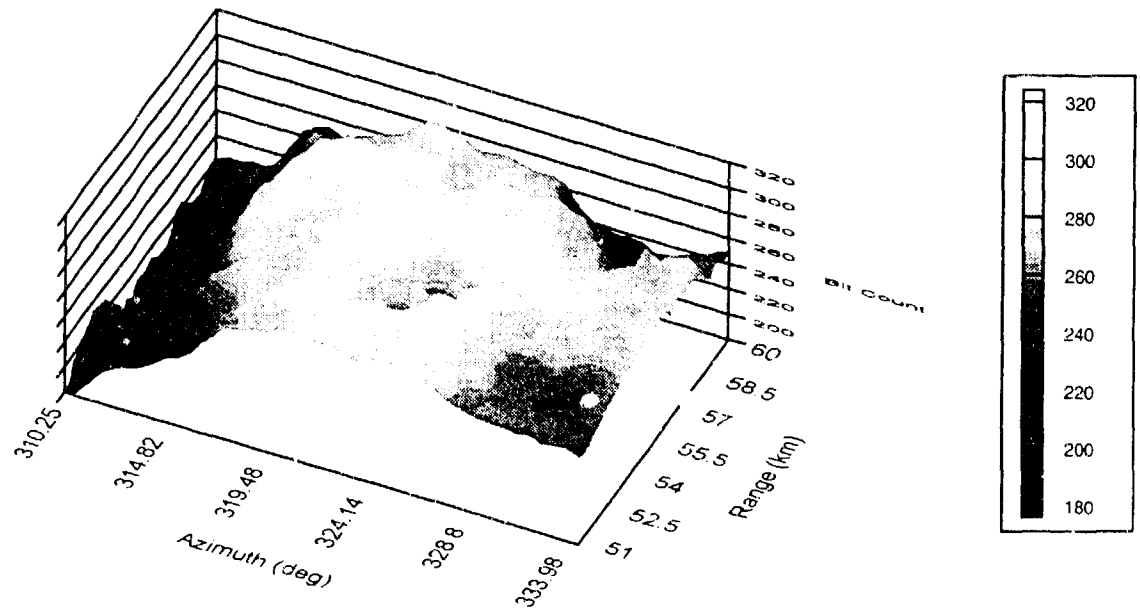

Figure 5. Three dimensional representation of the Control BWER. The BWER is centered about 54 km and 324°.

At the time of the control BWER, there were reports of three on the ground, one of which was anticyclonic. A mesocyclone and three TVS's (Tornado Vortex Signatures) were observed in the Doppler data at mid-levels. A BWER is seen for this control case centered 54 km and 324° from the radar. The elevation scans immediately above and below this scan show no evidence of a BWER. The 3° scan, though, does indicate a strong WER. The data collected before and after those presented here do not contain a BWER. This lack of temporal continuity is rather surprising in light of the severity of the associated weather at this time. It is therefore important that our identification schemes not be restricted to BWER identification, but should also include WERs.

Figure 6 depicts extrema identified by the pattern vector process for the Model BWER. This simple method yields the characteristic extrema distribution for an idealized BWERs. Each cell corresponding to a point on the reflectivity has been identified as an extremum (boxed and labeled 1) along with orthogonal crossing of extrema axes (labeled 1 but not boxed) centered on the BWER minima. It is

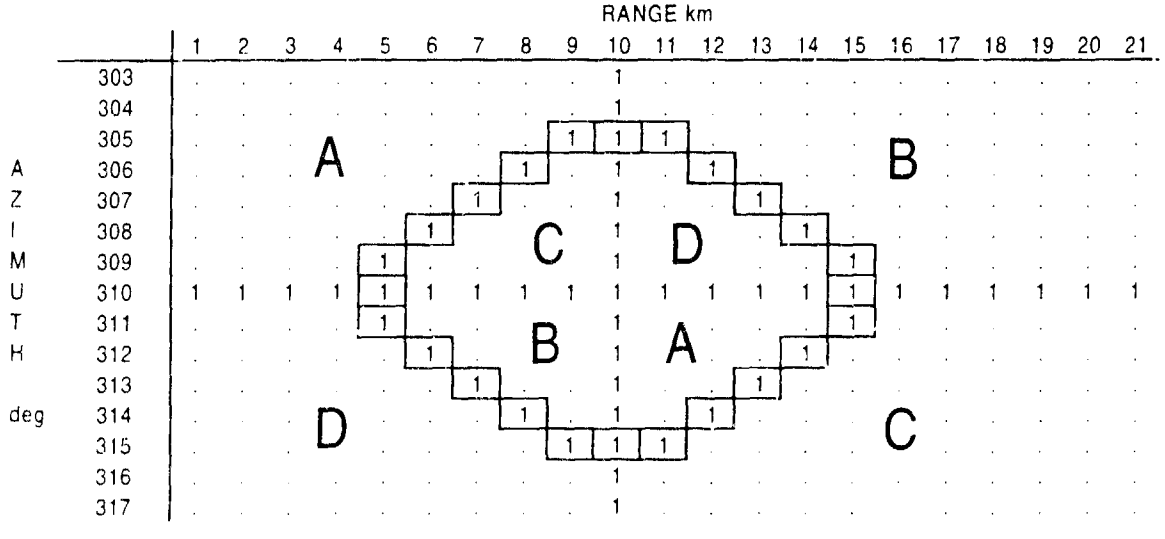

Figure 6. Model BWER extrema. Cells denoted 1 are extrema. The boxed cells reference the BWER ridge position. Regions A, B, C, D are discussed in the text.

important to remember that the extrema are the identified local maxima and minima after cross-range and cross-azimuth PV processing. From a pattern recognition perspective, processing this case is straightforward.

Additionally, the orthogonal axes for the extrema partition the regions inside and outside the BWER ridge into quadrants of differing reflectivity gradient characteristics. In Figure 6, the quadrants are labeled A-D. The distribution of the reflectivity gradient characteristics for the inside-BWER quadrants is a flipped mirror image of the quadrant arrangement outside the BWER. Quadrant A is observed to have positive reflectivity gradient both cross-range and cross-azimuth. Quadrant B

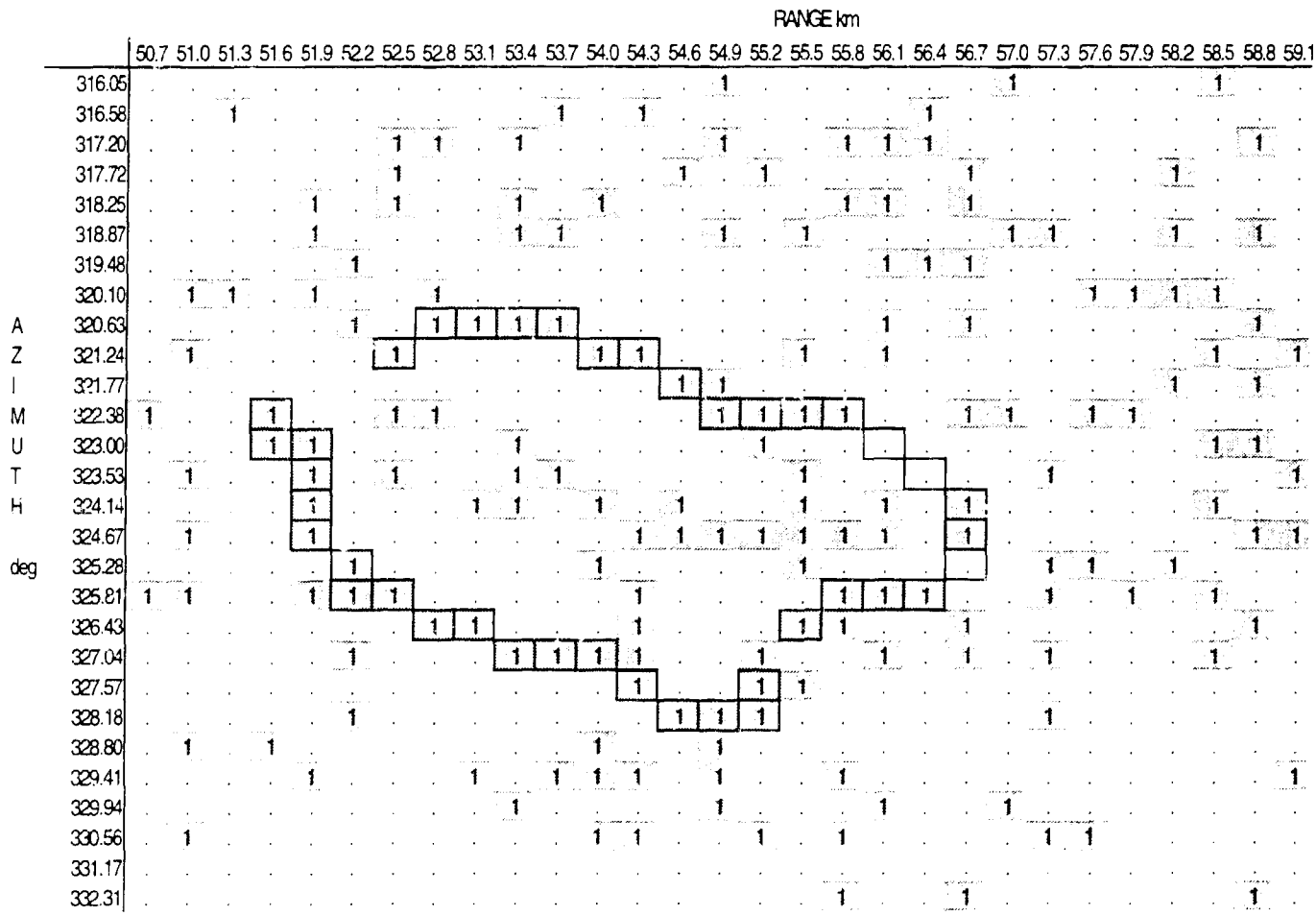

Figure 7. Extrema for the Control BWER are labeled one and shaded. The boxed cells reference the visually identified Control BWER ridge.

has a positive reflectivity gradient cross-azimuth with a negative reflectivity gradient cross-range. Quadrant C is noted to have negative reflectivity gradient in both process directions. Quadrant D has positive reflectivity gradient cross-range with negative reflectivity gradient cross-azimuth.

Figure 7 illustrates the results for the Control BWER from the same PV processing applied to the Model BWER. Here, extrema are dark shaded and labeled 1. The extrema distribution is quite noisy in this case. Note the large number of extrema identified individually and in clusters. The characteristic BWER extrema signature is not as apparent as with the model. Upon closer examination, extrema are associated with a significant section of the visually-determined BWER ridge (boxed cells in Figure 7) and some aspects of the orthogonal axes for the extrema can be found. In fact, 90% of those visually selected BWER cells had associated extrema. However, only 18% of all extrema were associated with the BWER. Thus, the extremum method provides a useful but incomplete product applicable to the delineation of the BWER. A careful study of the bit count values of Figure 2 reveals a quadrant organization of the reflectivity gradients similar to that for the model data (Figure 6). The next step is to develop techniques to enhance the BWER ridge and to discriminate against "noise" extrema.

2.5.4. Machine Intelligence and Parameter Sensitivity

As noted earlier, scientists at MIT Lincoln Laboratory designed the Machine Intelligent Gust Front Algorithm (MIGFA) based on visual radar characteristics of gust fronts. The fundamental concept for machine intelligent (MI) techniques was derived from military battle scene applications and involves the extraction of image characteristics through individual analyses of the original data for each characteristic. These independent characteristics are then combined through the use of scoring (i.e., weighting) functions. This approach is basically a parallel approach, where each analysis is independent of the other and uses the original data as a starting point. Conventional processing tends to be somewhat serial in that each step of the analysis is based on a product of a previous analysis procedure. Therefore, conventional processing will result in fewer independent products than the MI approach for assimilation into a comprehensive final product.

We have applied MI theory to the BWER identification problem. The baseline data are first modified to smooth outliers from the data. Different approaches, with and without scoring functions, are explored to combine independent characteristics of the data.

2.5.4.1.Additional Pattern Vector Information

The generation of extrema is one analysis in the MI approach. As this approach becomes more sophisticated, the extrema information will be combined with other independent analyses of the original, unprocessed data set. Before designing additional analyses, we must explore what additional information the extrema generation process provides. It yields more information than simple yes or no for extremum occurrence. As explained above, the extrema are found to be of cross-range, cross-azimuth, or dual (of both) types. Figure 8a and b show the Model BWER and Control BWER extrema, respectively, as noted earlier but now coded for type. In both figures, the location of the BWER ridge outline is indicated by the boxed cells. For the model, most of the ridge points as well as the minima (BWER center) are the dual type, meaning that both the cross-azimuth and cross-range methods identified them. Where the ridge has significant curvature, detection is accomplished with only one of the methods. The orthogonal axes through the center of the BWER are also of a single type. For the control case most of the extrema are of a single type. There are two minima in this case and these are designated as dual type as in the model. The occurrence of the control minima is a reflection of the complexity of the situation actually observed in nature.

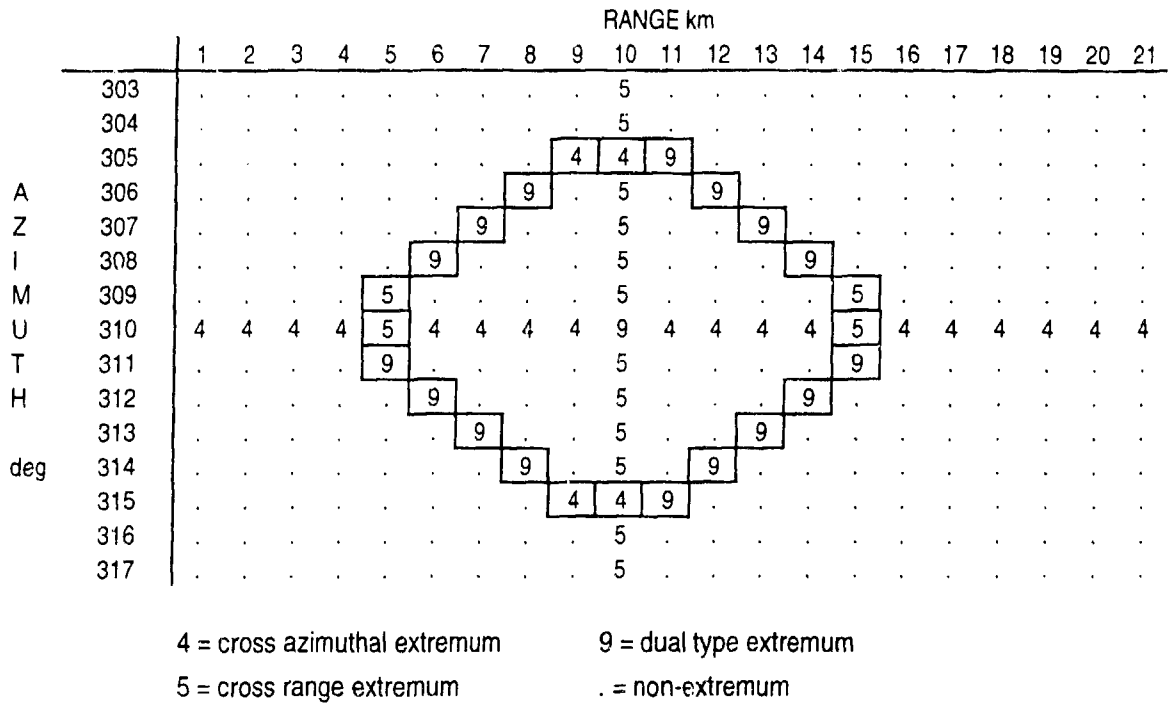

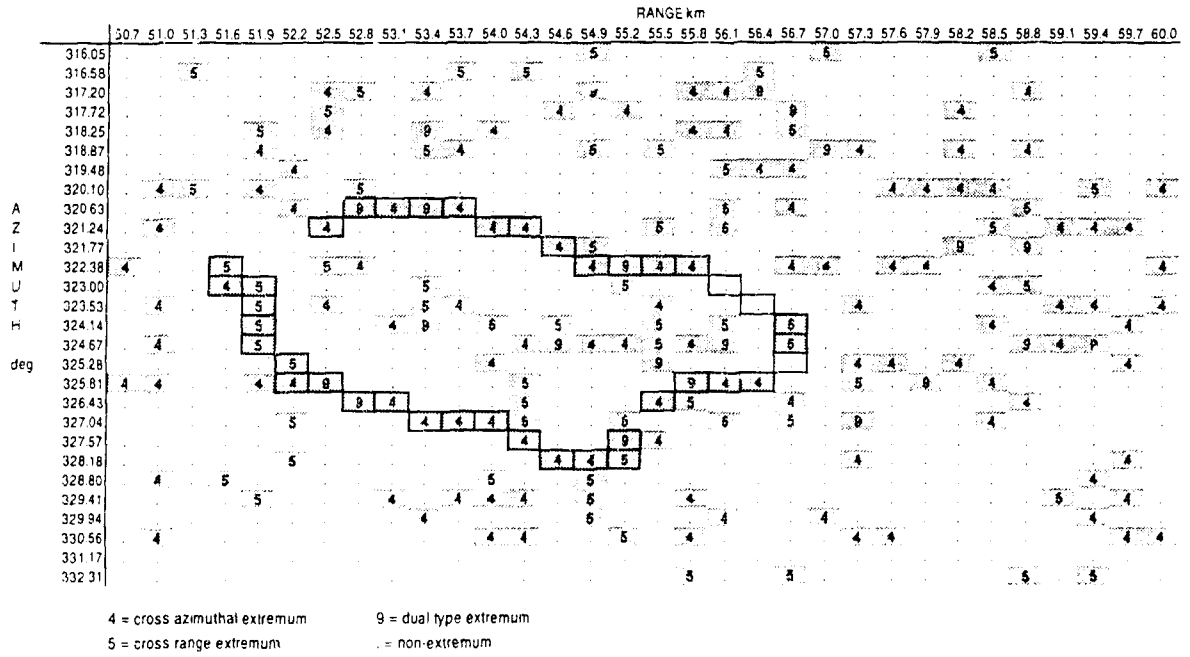

Figure 8. a) Model BWER and b) Control BWER extrema coded for type. Boxed cells reference the BWER ridge.

Another parameter related to the extrema is the length of the positive and negative pattern vectors used to identify each extremum. As discussed previously, the minimum PV cell length of either sign was required to be three (two links). Thus, the minimum combined length centered about the extremum would be five cells. The impact of increasing the minimum cell length of both positive and negative PVs on the identification of the BWER ridge points and reduction of the unnecessary "noise" extrema was examined. For the Control BWER, it was found that the identified percentage of BWER cells and total extrema rapidly decreased as the minimum PV cell length increased from three to six. This indicates that increasing the minimum PV cell length will result in reduced BWER definition.

In the above analyses, both PVs associated with an extremum were constrained to be of equal lengths. A less restrictive constraint would be that the PV lengths could be unequal but with a combined length that passes a minimum threshold. Table 1 shows the results of this exercise as applied to the Control BWER. As expected an increase in the lengths of PV pairs yields lower percentages of the BWER cells being identified and a reduction in the overall number of extrema. Of note, however, is that a single cell increase to six from the default minimum of five did not substantially impact the percentage of BWER cells identified while dropping 35 noise extrema. The cell requirements for cases A-F correspond to actual lengths of 1-3 km along the radial and 1.5-3.5 km across radials for the Control BWER case. To identify at least 75% of the BWER ridge cells (cases A-C), the PV paired-lengths are about 2 km. This is about a quarter of the BWER horizontal extent noted by Lemon (1977). It remains to be seen if 2 km is a realistic upper limit for BWER ridge detection with extrema. This is important for range resolution sensitivity because, obviously, the radial separation will be larger at greater ranges from the radar.

Table 1. Extrema Associated PV Paired-Length Sensitivity Analysis

CASE	A	B	C	D	E	F
extrema-associated cell length	5	6	7	8	9	10
BWER ridge extrema	36	35	31	27	23	20
% BWER ridge cells	90.0	87.5	77.5	67.5	57.5	50.0
Total extrema	201	166	128	105	71	51
% BWER extrema/Total	17.9	21.1	24.2	25.7	32.4	39.2
DUAL extrema	23	16	11	6	5	4
CROSS-RANGE extrema	69	56	38	35	20	12
CROSS-AZIMUTH extrema	109	94	79	64	46	35

In Table 1, it is observed that, for both the cross-range and cross-azimuth types, lengthening the PV pairs increases the percentage of extrema associated with the BWER ridge. We find that 30% of the non-BWER cross-azimuth extrema and 53% of the BWER ridge extrema have PV paired-lengths greater than 9 cells. For the cross-range extrema, the values are 21% and 44%, respectively. This type of information may prove useful for MI techniques.

2.5.4.2.Reflectivity Magnitude

As discussed, we require independent information for BWER identification to complement that from extrema and their attributes. Pattern vectors and extrema utilize the strong reflectivity gradients associated with BWERs. Another characteristic of BWERs is that they are located within high reflectivity regions. A natural independent parameter might be the reflectivity magnitude itself. MI theory allows that, with just two independent analyses of the same data, a combined

interest field can be generated. Combined interest implies that results from independent analyses are combined to yield a better description of the feature of interest than could be achieved from independent assessments.

An elementary MI combined interest array was created from an overlay of the Control BWER extrema array and the Control BWER reflectivity. The first step is to generate a binary thresholded reflectivity field where we assign 1 to any cell whose magnitude fits the threshold criteria and 0 to all others. We then multiply the extrema array by this binary array. To objectively compute a magnitude threshold, the reflectivity values (in bit counts) are ranked in descending order and, then, a specified top percentage is accepted. To test sensitivity, this percentage was varied. The data domain was also varied from an isolated region to the entire storm. Recall that the cells of the extrema array are assigned zeroes for non-extremum and a coded-integer value for extremum type. This means that the combined interest array has non-zero values only where extrema have reflectivity magnitudes above the threshold. Table 2 lists results for four tests for different domains and thresholds where outliers are filtered plus the non-MI result where there was no filtering for outliers. All of these analyses were performed on the Control BWER with a minimum PV paired-length of

Table 2. Simple Magnitude Combined Interest Results

CASE	A	B	C	D	E
RANK TYPE	entire	entire	high	high	none
MAG. RANK FILTER	10%	20%	20%	25%	none
BWER RIDGE EXTREMA	31	35	32	34	36
% BWER RIDGE EXTREMA	77.5	87.5	80.0	85.0	90.0
TOTAL EXTREMA	62	79	68	76	201
% BWER extrema/TOTAL	50.0	44.3	47.1	44.7	17.9

The RANK TYPE refers to the spatial domain over which the magnitude ranking is performed. Magnitudes are ranked in descending order based on the entire storm array or the high reflectivity box. The MAG. RANK FILTER shows the percentile used to determine the magnitude threshold applied to the rank type array. For instance, in Case A only cells whose magnitudes were in the top 10% are accepted. The percentage of the BWER ridge cells that are detected does not exhibit a clear relationship with the magnitudes of either the threshold or the domain. On the other hand, there is evidence that a greater percentage of extrema are associated with the BWER when there is at least some thresholding. This improvement is the result of a significant reduction of noise. This simple MI approach illustrates that significant improvements are possible with this technique. Figure 9 shows the resultant extrema pattern for the Control BWER after application of this simple MI approach for Case B along with the visually identified BWER ridge as denoted by boxed cells. Refer to Figure 7 for the non-MI (Case E) depiction for comparison. Case A yielded the best BWER ridge to total extremum percentage but

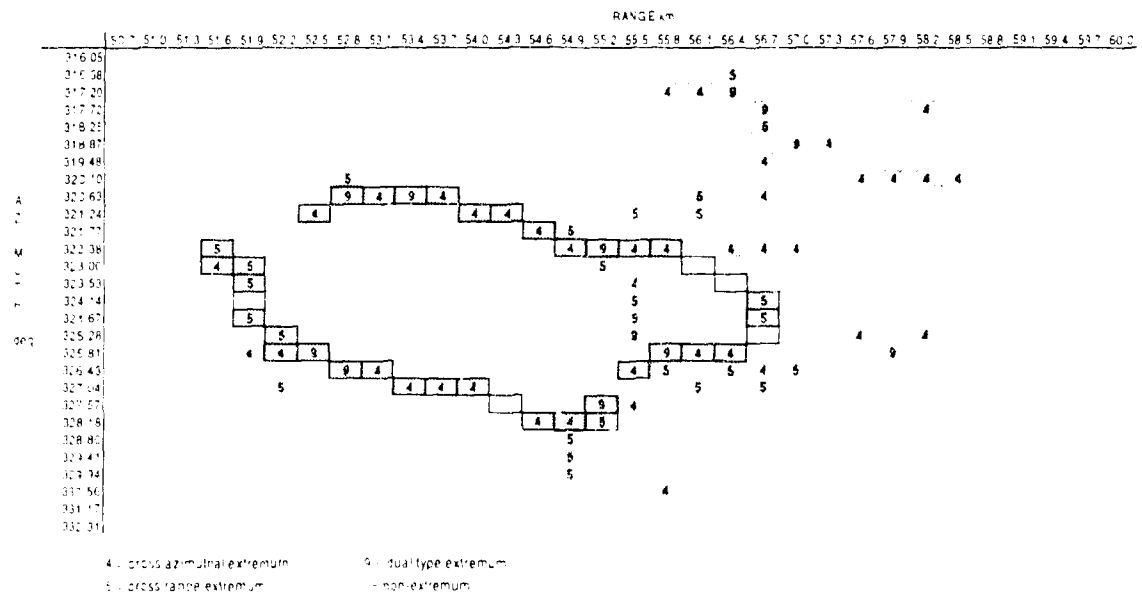

Figure 9. Extrema remaining after simple MI technique applied to the Control BWER. Extrema are number coded by type and shaded. The boxed cells correspond to the visually selected Control BWER ridge.

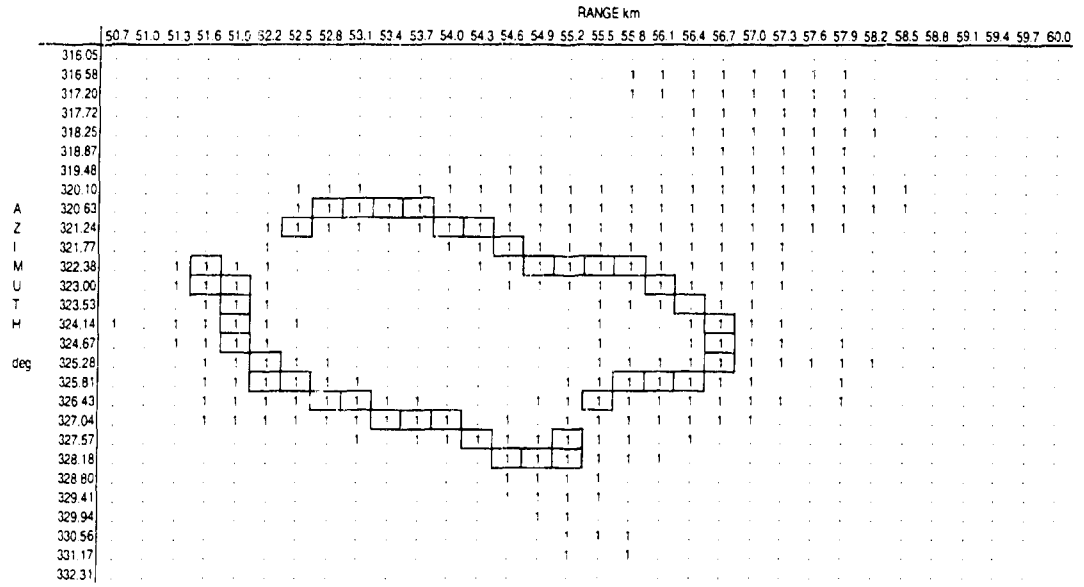

Figure 10. Top 20 percent reflectivity magnitude for the Control BWER. Boxed cells as in Figure 9.

the lowest percentage BWER ridge identified. It appears that if the descending magnitude rank is to be applied only to the high reflectivity box identified in preprocessing, a larger percentage of the descending rank order must be accepted to yield similar results (see Case D).

To this point, a simple MI approach has resulted in the identification of the entire Model BWER ridge and a significant part of the Control BWER. This approach uses characteristics of the high reflectivity region, reflectivity gradient structure, and peak reflectivity data. In the control case, a large amount of the noise extrema has also been eliminated. All this was done without converting the bit count data and coordinates into real physical values, thus, keeping the computational load to a minimum. However, more information is needed to complete the BWER ridge and to discriminate against non-BWER extrema.

Figure 10 shows the binary coding of reflectivity magnitude for Case B. All but one of the visually selected BWER ridge points (the boxed cells) fall into the top

20% of the reflectivity (denoted as 1). Figure 9 and Figure 10 highlight some difficulties with extraction of the Control BWER ridge. The upper left of the BWER (gate 52.2 km and radial 321.77°) is not clearly defined. With the use of the magnitude filter a connection can be made in this area. This suggests that a more sophisticated or second application of the magnitude information might be useful. The right side of the Control BWER is another difficult region to detect. There are two possible boundaries in this region. One extends across the BWER at a range of 55.5 km while the other extends more to the right to a range of 56.7 km (Figure 10). However, there is not enough information to make an objective decision. The visual edge (far right) has higher magnitude but less associated extrema than does the closer edge. In effect there appears to be a structure analogous to a double sink. As mentioned earlier, data from adjacent elevations and volumes do not aid in the decision process here. It is possible that the BWER is in a dynamic state of change at this time. It is also possible that improved resolution might have detected the BWER at other elevations. The BWER may be expanding or contracting or a second BWER may be forming or decaying. It is apparent that there are other parameters that might help in this identification process.

Figure 11 is the simple combined MI approach of Case B after the data have been preprocessed for outliers. The coding for this figure is the same as for Figure 9. The results show that a few additional extrema are detected to fill some gaps along the BWER ridge but these do not resolve the larger feature issues. In this case, 37 of 82 extrema are along the BWER ridge. Additionally, the complex BWER structure noted in the previous paragraph is more strongly portrayed in this figure.

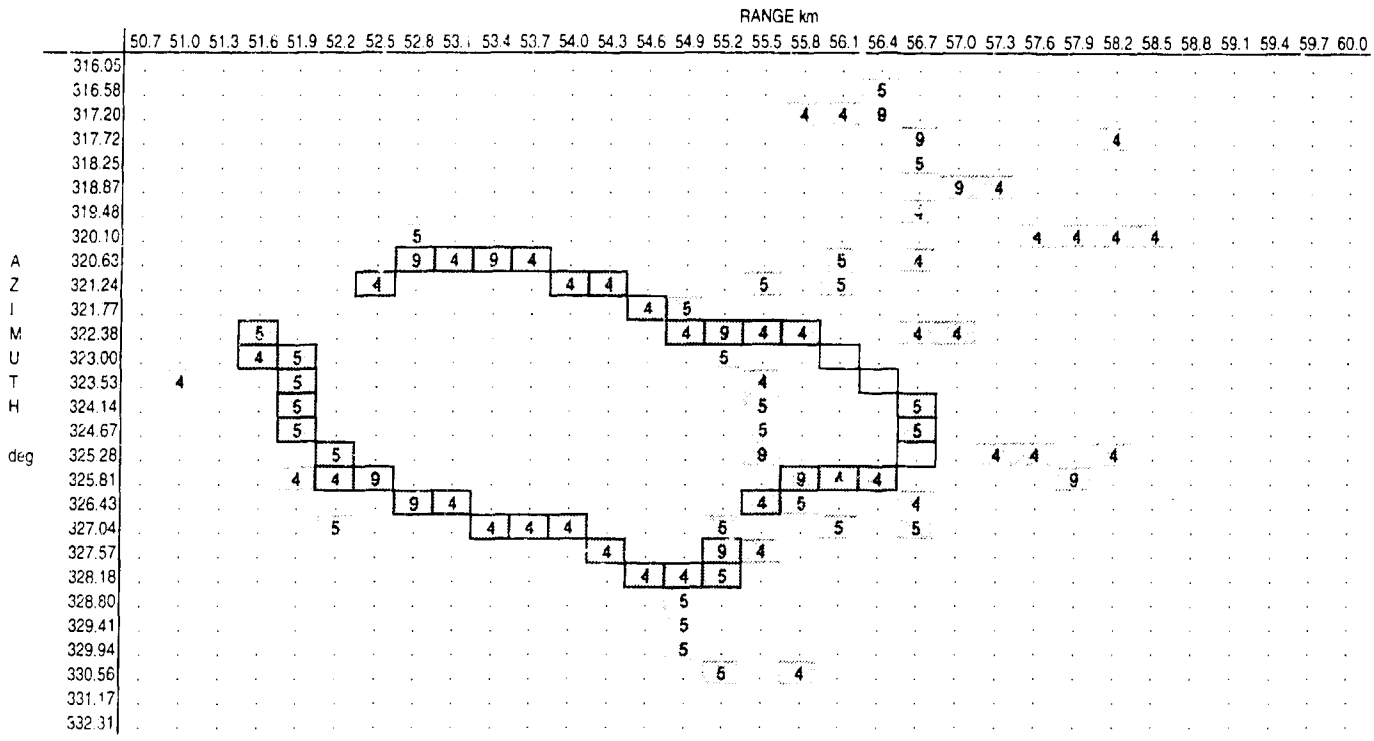

Figure 11. Extrema remaining after simple MI technique applied to the Control BWER after outlier processing. Cells are coded as in Figure 9.

Two additional issues are examined briefly at this juncture: the application of the simple MI approach to a WER case and the potential for the false detection of BWERs where there is a complex reflectivity structure. When the MI approach was applied to a WER, the method captured the essence of the WER from the scan previous to the Control BWER. Thus, the BWER techniques show promise for application to WER situations. However, due to the unbounded nature of WERs, the actual extraction of the border may be more complex. To evaluate the potential of false alarms, another simple model has been adopted where there are four reflectivity peak regions with a weaker reflectivity region between them. This is a simple attempt to mimic potential intra- or inter-storm situations. Application of the simple MI approach correctly yielded four sets of orthogonal extrema axes for each of the cells without identifying the center region between the peaks as a BWER. When a BWER was added to one of the reflectivity peaks, it was properly found.

2.5.4.3.Gradient Magnitude and Direction

The magnitude and direction of the gradients are important parameters available for MI analysis. We will first examine the nature of these parameters relative to the BWER. It has been established that the BWER ridge is composed primarily of extrema where the gradient magnitude is at or near zero. Because of data sampling and resolution limitations, it is unlikely that the estimated gradient magnitude will be zero, but it should be relatively.

Several pattern recognition templates have been developed to compute the orthogonal components (Nadler and Smith, 1993) used to calculate the gradient magnitude and direction. The Sobel operator was selected for this since it is regarded as a solid performer and is elementary to apply. Figure 12 shows the orthogonal Sobel gradient operators that are applied to the Control and Model BWER data. With this operator, the value for the target cell is not used in the computation of the x and y components. Additionally, the Sobel operator applies a double weight to the cells either along the radial or at a common range across radials and a weight of one to the corner cells. A comparison of the results from the application of the Sobel operator with those from a linear operator (all cells are equal weighted), indicated that the magnitudes were larger from the Sobel computations but the directions were qualitatively equivalent. Since the relative distribution of the gradient is similar in the results for the two operators, the choice of a linear or Sobel operator appears to be of minor importance.

SOBEL GRADIENT OPERATOR

1	2	1
	TC	
-1	-2	-1

ΔX

-1		1
-2	TC	2
-1		1

ΔY

Figure 12. The orthogonal component templates of the Sobel operator.

AZIMUTH deg \ RANGE km	1	2	3	4	5	6	7	8	9	10	11	12	13	14	15	16	17	18	19	20
300																				
301		67.88	67.88	80.00	83.23	73.76	73.76	73.76	62.48	48.00	62.48	73.76	73.76	73.76	83.23	80.00	67.88	67.88	67.88	67.88
302		67.88	67.88	80.00	83.23	73.76	73.76	73.76	62.48	48.00	62.48	73.76	73.76	73.76	83.23	80.00	67.88	67.88	67.88	67.88
303		67.88	67.88	80.00	83.23	73.76	73.76	73.76	62.48	48.00	62.48	73.76	73.76	73.76	83.23	80.00	67.88	67.88	67.88	67.88
304		80.00	80.00	89.10	90.61	82.07	82.07	82.07	67.96	54.00	67.96	82.07	82.07	82.07	90.61	89.10	80.00	80.00	80.00	80.00
305		83.23	83.23	90.61	91.92	85.04	85.04	66.71	**22.80**	**2.00**	**22.80**	66.71	85.04	85.04	91.92	90.61	83.23	83.23	83.23	83.23
306		73.76	73.76	82.07	85.04	79.20	60.81	**2.83**	54.20	68.00	54.20	**2.83**	60.81	79.20	85.04	82.07	73.76	73.76	73.76	73.76
307		73.76	73.76	82.07	85.04	60.81	**1.41**	63.66	87.01	74.00	87.01	63.66	**1.41**	60.81	85.04	82.07	73.76	73.76	73.76	73.76
308		73.76	73.76	82.07	66.71	**2.83**	63.66	93.34	95.13	76.00	95.13	93.34	63.66	**2.83**	66.71	82.07	73.76	73.76	73.76	73.76
309		62.48	62.48	67.96	**22.80**	54.20	87.01	95.13	90.51	64.00	90.51	95.13	87.01	54.20	**22.80**	67.96	62.48	62.48	62.48	62.48
310		48.00	48.00	54.00	**2.00**	68.00	74.00	76.00	64.00	0.00	64.00	76.00	74.00	68.00	**2.00**	54.00	48.00	48.00	48.00	48.00
311		62.48	62.48	67.96	**22.80**	54.20	87.01	95.13	90.51	64.00	90.51	95.13	87.01	54.20	**22.80**	67.96	62.48	62.48	62.48	62.48
312		73.76	73.76	82.07	66.71	**2.83**	63.66	93.34	95.13	76.00	95.13	93.34	63.66	**2.83**	66.71	82.07	73.76	73.76	73.76	73.76
313		73.76	73.76	82.07	85.04	60.81	**1.41**	63.66	87.01	74.00	87.01	63.66	**1.41**	60.81	85.04	82.07	73.76	73.76	73.76	73.76
314		73.76	73.76	82.07	85.04	79.20	60.81	**2.83**	54.20	68.00	54.20	**2.83**	60.81	79.20	85.04	82.07	73.76	73.76	73.76	73.76
315		83.23	83.23	90.61	91.92	85.04	85.04	66.71	**22.80**	**2.00**	**22.80**	66.71	85.04	85.04	91.92	90.61	83.23	83.23	83.23	83.23
316		80.00	80.00	89.10	90.61	82.07	82.07	82.07	67.96	54.00	67.96	82.07	82.07	82.07	90.61	89.10	80.00	80.00	80.00	80.00
317		67.88	67.88	80.00	83.23	73.76	73.76	73.76	62.48	48.00	62.48	73.76	73.76	73.76	83.23	80.00	67.88	67.88	67.88	67.88
318		67.88	67.88	80.00	83.23	73.76	73.76	73.76	62.48	48.00	62.48	73.76	73.76	73.76	83.23	80.00	67.88	67.88	67.88	67.88
319		67.88	67.88	80.00	83.23	73.76	73.76	73.76	62.48	48.00	62.48	73.76	73.76	73.76	83.23	80.00	67.88	67.88	67.88	67.88

AZIMUTH deg \ RANGE km	50.7	51.0	51.3	51.6	51.9	52.2	52.5	52.8	53.1	53.4	53.7	54.0	54.3	54.6	54.9	55.2	55.5	55.8	56.1	56.4	56.7	57.0	57.3	57.6	57.9	58.2	58.5	58
310.25																												
310.87		131.53	96.18	76.42	73.50	77.01	46.52	98.95	36.06	26.42	57.27	46.67	51.24	51.48	41.01	43.27	46.24	50.22	52.15	73.17	105.54	118.41	100.86	62.35	56.13	61.40	67.01	80.
311.40		82.37	42.05	41.88	59.46	39.40	50.36	86.37	26.08	24.17	53.74	62.82	72.12	58.55	56.04	80.11	76.90	64.28	71.85	98.68	111.33	107.84	87.69	74.97	74.69	72.80	79.76	81.
312.01		31.62	45.10	50.70	31.14	21.54	70.26	54.59	31.62	45.01	66.29	74.43	67.47	67.08	83.20	105.99	96.19	87.05	89.84	96.18	79.12	66.48	69.58	74.73	78.79	72.80	65.51	53
312.54		24.70	64.40	55.01	13.42	32.25	60.53	41.62	59.41	77.67	81.06	78.09	68.03	74.24	94.24	93.48	73.01	72.44	74.09	69.35	53.85	51.26	57.58	65.80	71.55	62.43	33.02	22.
313.15		54.41	76.42	38.29	9.49	25.02	38.21	53.08	65.15	68.95	67.07	75.54	78.41	72.57	73.35	61.74	47.01	46.69	46.52	44.41	34.21	26.00	30.53	23.02	43.08	40.50	20.00	24.
313.68		61.74	55.61	22.09	25.50	25.02	57.43	67.01	52.17	38.47	38.83	51.98	81.77	83.53	70.65	53.37	50.04	56.32	52.95	41.23	19.24	8.25	27.02	32.89	47.71	19.65	24.17	42.
314.30		41.18	29.19	22.85	37.91	69.35	88.54	90.20	79.76	60.13	70.68	86.03	89.22	96.08	106.17	100.08	90.20	105.57	111.11	84.59	59.48	41.88	16.55	14.14	21.21	40.05	59.67	81.
314.62		40.79	33.11	37.66	58.26	100.00	111.89	109.55	101.24	99.13	117.18	110.16	102.90	107.36	124.11	129.87	121.00	124.19	126.76	126.85	127.02	118.59	96.72	81.74	91.44	85.05	80.99	98.
315.44		50.64	52.85	61.57	76.12	100.52	96.66	78.10	84.86	105.65	117.00	95.35	89.11	96.06	96.14	83.55	81.50	78.00	72.25	94.59	122.06	146.16	152.95	145.17	129.00	101.19	68.41	71.
316.05		57.71	56.14	61.74	67.86	76.38	76.17	51.42	66.41	93.21	79.71	63.07	51.92	51.88	37.95	30.89	39.01	55.05	58.55	69.18	79.17	101.96	131.85	136.53	123.98	115.38	66.75	46.
316.58		69.07	58.14	58.31	55.82	61.33	72.53	44.00	49.40	53.82	28.28	20.25	15.23	12.17	17.03	5.10	35.38	50.48	58.31	67.19	60.53	46.32	48.85	53.37	70.21	104.69	77.25	52.
317.20		58.19	54.59	64.51	54.41	46.86	46.04	13.04	15.81	26.08	21.26	14.42	12.00	17.26	19.24	24.04	43.66	34.00	37.34	29.73	34.99	32.56	23.02	12.81	24.70	75.60	65.51	50.
317.72		40.51	44.38	53.24	48.17	21.02	24.41	39.12	27.89	27.46	27.02	10.02	7.13	0.60	8.00	7.75	37.51	46.86	63.70	68.54	4.47	34.21	32.80	27.31	19.65	45.65	51.25	53.
318.25		36.14	36.69	35.38	31.62	45.28	27.17	28.32	14.14	12.00	29.02	6.78	9.49	19.00	19.03	14.71	11.05	14.71	46.52	82.22	29.15	16.55	24.21	25.50	25.02	46.65	59.93	50.
318.87		22.08	20.10	21.95	30.89	45.03	58.41	57.79	53.31	36.00	46.75	29.54	25.16	41.83	31.62	24.77	13.47	13.65	27.02	69.64	49.66	10.20	5.00	19.70	51.01	53.85	44.92	26.
319.48		12.65	7.07	15.23	36.50	21.63	38.21	44.85	51.11	49.09	56.30	34.93	33.02	43.93	34.67	41.59	43.93	41.01	41.79	55.57	42.75	7.62	8.49	11.31	57.27	64.40	56.57	35.
320.10		18.60	12.00	22.67	28.46	22.67	25.79	30.90	42.54	47.52	49.40	45.89	44.00	23.41	16.97	25.50	39.22	52.95	65.97	55.95	25.61	12.00	12.08	5.10	35.36	43.91	55.01	26.
320.63		6.32	21.02	24.70	24.04	18.87	34.06	**19.24**	**15.56**	**18.60**	**28.32**	38.47	42.38	30.46	24.04	15.81	22.36	34.41	26.42	7.07	15.23	20.00	20.10	36.50	48.37	51.40	53.01	22.
321.24		17.03	25.61	17.72	21.40	7.62	**22.80**	42.94	37.12	36.88	46.04	**38.29**	**10.00**	24.00	52.15	62.82	43.57	27.46	4.24	29.15	33.29	32.56	39.22	51.26	63.07	69.77	42.45	10.
321.77		27.46	38.18	37.01	26.68	22.36	42.94	57.57	55.01	58.03	69.57	75.17	44.94	**34.06**	46.67	57.27	54.42	25.50	10.20	35.69	35.69	20.88	33.97	41.23	48.17	39.70	25.50	24.
322.38		32.56	47.01	**34.21**	36.06	59.68	48.85	33.11	47.54	67.60	73.38	81.22	73.65	71.06	**65.80**	**33.14**	**43.84**	**26.83**	16.12	38.63	40.45	10.20	27.46	33.90	27.77	17.30	6.32	20.
323.00		42.06	43.89	**24.08**	**20.25**	39.94	59.08	16.49	59.41	60.17	62.61	74.97	78.60	95.02	108.05	88.21	76.54	52.61	**34.97**	33.84	22.25	17.09	26.31	31.85	28.60	21.59	17.03	6.3
323.53		62.64	37.12	36.06	**4.47**	94.35	69.63	24.98	66.21	20.25	33.73	43.08	55.32	93.61	109.83	74.32	37.01	35.44	38.63	**8.25**	13.72	21.21	20.88	23.86	30.81	26.33	27.20	19.
324.14		86.39	42.34	38.05	**5.10**	72.60	74.67	54.19	58.19	22.00	33.11	11.42	49.74	55.46	81.30	68.35	17.26	22.67	43.04	29.49	**16.97**	25.61	24.21	18.38	25.50	25.61	40.45	23.
324.67		71.12	51.09	33.05	**7.07**	46.74	77.19	85.21	83.87	47.41	4.47	23.02	26.57	41.11	74.63	84.20	42.45	51.40	46.75	40.25	**14.76**	24.08	27.02	22.36	25.06	30.89	53.24	23.
325.28		21.40	49.01	45.01	22.67	**47.52**	86.16	106.00	100.77	77.79	39.82	17.20	20.40	69.34	83.76	81.84	51.07	66.29	63.20	29.73	**15.03**	31.40	23.02	3.16	15.56	45.01	50.16	23.
325.81		11.40	36.69	53.11	39.29	**22.36**	**28.46**	68.12	90.21	88.09	94.02	71.55	49.82	86.83	81.22	55.57	52.35	**8.60**	**17.09**	**8.25**	28.98	43.36	33.62	37.29	11.40	59.41	36.06	26.
326.43		44.72	41.40	49.19	54.41	48.76	49.01	**45.45**	**54.04**	43.86	84.86	104.31	80.62	90.34	67.54	35.57	**26.08**	34.00	44.94	26.31	25.90	55.81	32.31	40.47	28.07	46.84	24.70	45.
327.04		54.92	59.43	54.92	62.67	65.97	69.18	63.20	45.65	**23.71**	**2.83**	**53.54**	46.69	53.45	47.43	28.03	12.73	30.00	33.62	36.29	44.06	62.23	31.34	28.54	47.07	41.76	20.25	67.
327.57		51.88	72.24	59.77	66.20	68.25	67.36	65.10	61.20	63.95	67.47	42.99	**23.77**	35.61	40.67	**5.39**	29.83	37.44	25.81	34.05	54.20	43.83	19.80	25.01	41.61	34.81	31.14	81.
328.18		49.82	65.78	55.84	50.92	69.07	75.06	73.17	68.12	61.40	70.26	70.67	64.62	**41.04**	**25.50**	**21.02**	40.50	38.83	35.61	30.74	45.10	28.48	17.09	24.14	18.38	18.83	49.98	106
328.80		18.11	48.76	46.69	43.29	50.99	51.09	48.17	44.94	34.18	35.44	64.21	89.50	52.56	24.70	25.06	41.88	45.61	28.43	16.40	42.45	23.03	19.65	20.69	31.11	62.29	92.66	113
329.41		5.83	24.17	37.20	27.02	20.25	15.23	13.90	24.41	25.30	12.65	53.76	75.06	51.87	21.40	21.40	40.25	38.53	10.00	8.91	53.25	28.54	44.18	60.75	77.18	92.31	84.02	62.
329.94		3.16	6.00	21.21	19.65	15.33	15.03	18.87	25.50	40.02	37.20	52.33	46.84	40.30	33.40	17.75	29.43	32.65	15.62	16.55	55.79	46.07	56.80	81.18	77.08	66.47	46.04	27.
330.56		7.07	12.81	17.20	22.09	28.07	28.28	30.00	46.39	47.85	38.91	28.64	19.02	26.50	41.18	9.30	18.11	24.70	24.70	27.17	43.93	50.99	58.94	44.73	42.54	43.01	39.70	39.
331.17		14.00	13.04	11.66	17.20	22.36	28.28	44.05	68.35	48.33	39.12	31.24	29.12	31.45	44.79	43.73	37.34	30.23	32.65	33.29	27.20	29.83	75.01	94.27	97.00	57.59	41.52	39.
332.31		14.56	6.00	4.47	15.81	14.21	17.49	38.60	77.83	75.49	58.05	34.44	40.00	48.75	50.70	61.07	63.20	67.19	58.46	40.72	26.42	10.00	25.61	56.32	116.18	122.61	73.66	52.
332.84		13.42	13.42	12.55	12.02	12.58	16.12	14.42	32.56	60.75	60.73	19.24	27.31	41.18	37.36	28.28	38.47	52.55	36.06	6.94	9.49	11.40	1.41	3.16	63.18	111.12	102.90	89.
333.46		13.42	10.77	26.20	10.00	20.18	38.83	43.17	38.63	49.66	53.01	10.30	13.42	11.66	19.70	3.16	15.81	24.11	25.61	13.42	7.07	7.07	4.24	8.25	27.39	76.49	68.44	52.
333.98		28.07	28.46	11.92	24.01	27.28	29.43	33.38	35.47	39.62	31.05	7.21	3.16	17.49	21.26	7.21	7.21	14.14	11.05	22.09	26.83	23.19	24.33	29.15	37.91	61.06	52.87	10.

Figure 13. The gradient magnitude for a) the Model BWER and b) the Control BWER as computed from the Sobel operator. The shaded cells refer to the BWER ridge. Note that lower values are associated with the ridge cells.

RANGE km

AZIMUTH deg	1	2	3	4	5	6	7	8	9	10	11	12	13	14	15	16	17	18	19	20
300																				
301		0	0	0	0	0	0	0	0	0	1	1	1	1	1	1	1	1	1	1
302		0	0	0	0	0	0	0	0	0	1	1	1	1	1	1	1	1	1	1
303		0	0	0	0	0	0	0	0	0	1	1	1	1	1	1	1	1	1	1
304		0	0	0	0	0	0	0	0	0	1	1	1	1	1	1	1	1	1	1
305		0	0	0	0	0	0	0	0	1	1	1	1	1	1	1	1	1	1	1
306		0	0	0	0	0	0	0	1	1	0	1	1	1	1	1	1	1	1	1
307		0	0	0	0	0	0	1	1	1	0	0	1	1	1	1	1	1	1	1
308		0	0	0	0	0	1	1	1	1	0	0	0	1	1	1	1	1	1	1
309		0	0	0	0	1	1	1	1	1	0	0	0	0	1	1	1	1	1	1
310		0	0	0	1	1	1	1	1	1	0	0	0	0	0	1	1	1	1	1
311		0	0	0	0	1	1	1	1	0	0	0	0	0	1	1	1	1	1	1
312		0	0	0	0	0	1	1	1	0	0	0	0	1	1	1	1	1	1	1
313		0	0	0	0	0	0	1	1	0	0	0	1	1	1	1	1	1	1	1
314		0	0	0	0	0	0	0	1	0	0	1	1	1	1	1	1	1	1	1
315		0	0	0	0	0	0	0	0	0	1	1	1	1	1	1	1	1	1	1
316		0	0	0	0	0	0	0	0	1	1	1	1	1	1	1	1	1	1	1
317		0	0	0	0	0	0	0	0	1	1	1	1	1	1	1	1	1	1	1
318		0	0	0	0	0	0	0	0	1	1	1	1	1	1	1	1	1	1	1
319		0	0	0	0	0	0	0	0	1	1	1	1	1	1	1	1	1	1	1
320																				

0=NORTH COMPONENT
1=SOUTH COMPONENT

RANGE km

AZIMUTH deg	1	2	3	4	5	6	7	8	9	10	11	12	13	14	15	16	17	18	19	20
300																				
301		1	1	1	1	1	1	1	1	1	1	1	1	1	1	1	1	1	1	1
302		1	1	1	1	1	1	1	1	1	1	1	1	1	1	1	1	1	1	1
303		1	1	1	1	1	1	1	1	1	1	1	1	1	1	1	1	1	1	1
304		1	1	1	1	1	1	1	1	1	1	1	1	1	1	1	1	1	1	1
305		1	1	1	1	1	1	1	1	0	1	1	1	1	1	1	1	1	1	1
306		1	1	1	1	1	1	1	0	0	0	1	1	1	1	1	1	1	1	1
307		1	1	1	1	1	1	0	0	0	0	0	1	1	1	1	1	1	1	1
308		1	1	1	1	1	0	0	0	0	0	0	0	1	1	1	1	1	1	1
309		1	1	1	1	0	0	0	0	0	0	0	0	0	1	1	1	1	1	1
310		0	0	0	1	1	1	1	1	0	0	0	0	0	0	1	1	1	1	1
311		0	0	0	0	1	1	1	1	1	1	1	1	1	0	0	0	0	0	0
312		0	0	0	0	0	1	1	1	1	1	1	1	0	0	0	0	0	0	0
313		0	0	0	0	0	0	1	1	1	1	1	0	0	0	0	0	0	0	0
314		0	0	0	0	0	0	0	1	1	1	0	0	0	0	0	0	0	0	0
315		0	0	0	0	0	0	0	0	1	0	0	0	0	0	0	0	0	0	0
316		0	0	0	0	0	0	0	0	0	0	0	0	0	0	0	0	0	0	0
317		0	0	0	0	0	0	0	0	0	0	0	0	0	0	0	0	0	0	0
318		0	0	0	0	0	0	0	0	0	0	0	0	0	0	0	0	0	0	0
319		0	0	0	0	0	0	0	0	0	0	0	0	0	0	0	0	0	0	0
320																				

0=EAST COMPONENT
1=WEST COMPONENT

Figure 14. The binary North/South (a) or East/West (b) coding of gradient direction for the Model BWER. The boxed cells reference the BWER ridge. Note that portions of the ridge lie along transitions in the coded data.

As expected, the gradient magnitudes are the smallest in the Model B-scan for the cells forming the BWER ridge (see Figure 13a). Again, the Control BWER (Figure 13b) represents a dynamic, convoluted situation and is not nearly as well behaved as the model. To demonstrate this, consider how much of the BWER ridge for the Control and Model cases is detected for various gradient thresholds. For the Control BWER, the top 25% gradient magnitude threshold accounted for only 57.5% of the visual BWER and even the top 50% accounted for only 87.5%. By contrast, the top 5% gradient magnitudes for the Model BWER accounted for 100% of the ridge points. Indications from the control case are that the gradient magnitude approach may have limited application. However, it still may be a useful contributor to a total MI approach.

The gradient direction parameter is also examined. With the Sobel operator, the gradient direction is computed and reoriented relative to north. The extrema separate regions of different gradient direction. To facilitate analysis, the data are coded into octants and also into quadrants. The quadrant data are then binary-coded in terms of east-west and north-south components. Figure 14 shows typical coded patterns for the well-behaved Model BWER. Figure 15 shows the same for the Control BWER where there is much more variation than the model case. We can see from these figures that gradient directions better define the BWER ridge than gradient magnitudes (Figure 13) . However, this parameterstill does not resolve the ambiguities on the right side of the Control BWER.

It is important to note that these results, while encouraging particularly for the gradient direction signatures, are based on the use of the Sobel operator on the data in a B-scan format. This essentially gives equal weighting to cross-range and cross-azimuth components. At increasing range from the radar, the artificial nature of this gradient magnitude and direction technique may be more problematic. Therefore, it is intended that true gradient calculations will be made for the Control BWER and applied similarly to verify the utility of using the Sobel operator instead. Additionally, a range resolution check on this technique will be performed.

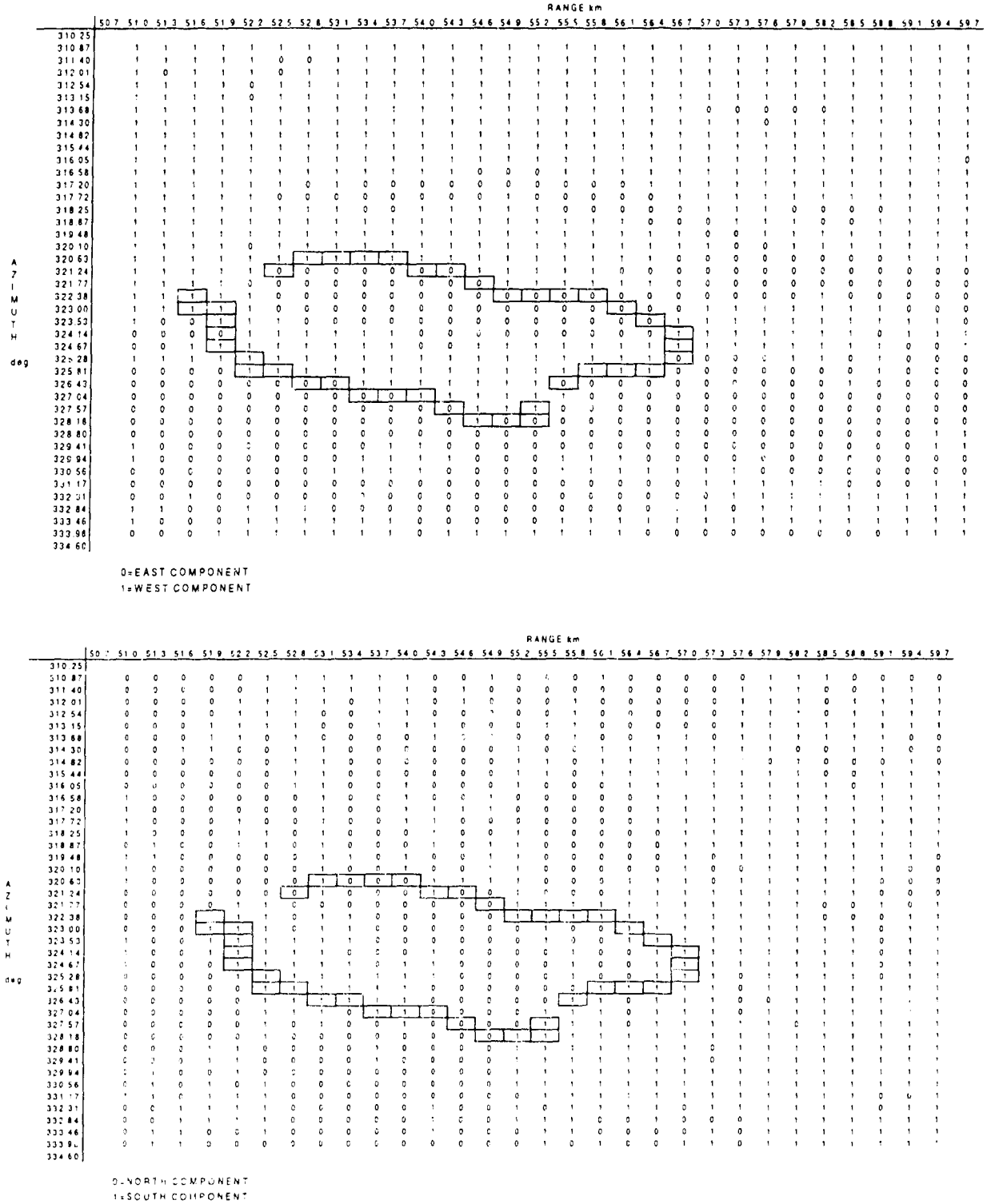

Figure 15. The binary North/South (a) or East/West (b) coding of gradient direction for the Control BWER. The boxed cells reference the BWER ridge. Note that portions of the ridge lie along transitions in the coded data.

2.6. *Current Research Efforts*

2.6.1. Scoring Functions/Machine Intelligence

As discussed previously, the MIGFA from MIT-Lincoln Laboratory yielded impressive results as a feature detection technique. It relies on scoring functions to emphasize the particular feature of interest. These scoring functions were applied via information from functional templates. The templates keyed on spatial relationships of features. The templates and scoring functions were coordinated such that maximum weighting was given for regions in the scene that most closely fit each template. The results of these various operations were then combined in a successful attempt to isolate the gust front.

Because BWERs are structurally and meteorologically quite different from gust fronts, the MIGFA is not directly transferable to our problem. However, from the previous discussions, there is ample evidence of useful information beyond the extrema that can be used in a MI approach to bolster the BWER signal. The current state of the research is geared to incorporate these other parameters in an intelligent and, ultimately, successful manner for BWER identification.

Two separate MI approaches are being explored beyond the simple magnitude approach discussed previously. The first involves methods similar to those used for the MIGFA. A 25 cell template (5 radials X 5 gates) centered on a target cell associated with two scoring functions was designed (see Figure 16). This template approximates a 1.5 km by 1.2 km region. The intent is to exploit the high reflectivity associated with the BWER ridge points and the surrounding reflectivity gradient. Scoring function 1 applies to the magnitude and scoring function 2 applies to the gradient. The scheme of each function is purely empirical with respect to the Control BWER so as to assess if there is any validity to this approach for this task.

SCORING FUNCTIONS AND TEMPLATES

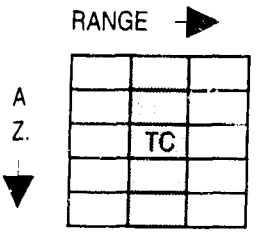

TC template centered on target cell

apply SCORING FUNCTION 2

apply SCORING FUNCTION 1

Scoring Function 1

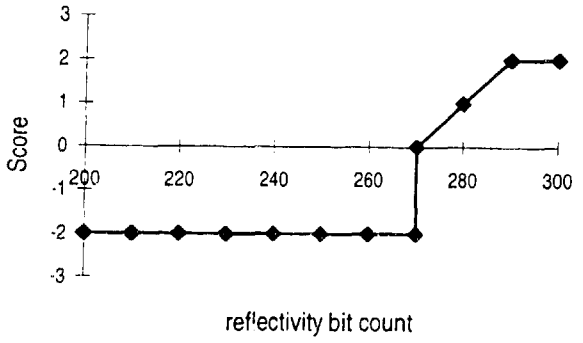

Scoring Function 2

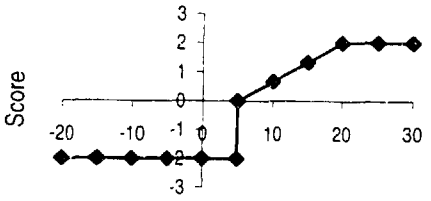

1) apply scoring function 1 to each dark shaded cell including the target cell to determine their individual score based on the reflectivity bit count

2) apply scoring function 2 to each light shaded cell by calculating the difference in reflectivity bit count from the target cell to determine their individual score

3) sum the scores from all the cells impacted by the template, divide by 11, and assign this average to the target cell

4) apply steps 1-3 across the entire reflectivity B-scan array then threshold these values to enhance image

Figure 16. A scoring function template and two scoring functions used in a different MI approach (see text for more details).

The template was applied across the B-scan array and an acceptance threshold applied. The results are shown in Figure 18. The accepted cells are labeled "1" while the boxed cells in the figure represent the visual BWER outline. When two basic BWER characteristics (reflectivity magnitude and gradient) are extracted, 67.5% of the BWER ridge cells are identified. However, those points account for only 24.7% of all selected points. This low percentage appears to be caused by a relatively thick BWER ridge. That is, many points adjacent to the BWER points are also selected via the template and scoring functions. While not conclusive in and of itself, this method suggests that, with additional templates rooted in other parameters and more observations on which to base the templates, results should be improved.

A second MI approach was examined. In this case, three feature-related normalized quantities with simple scoring functions are combined. Figure 17 shows the three scoring functions, all based on relative relationships of the parameters. The first scoring function uses a scale of 0-1 to cover from the lowest (least important) to the highest (most important) reflectivity magnitudes in the array. The second function is an accumulation of normalized extremum-associated PV paired-lengths. For cross-range extrema, the longest paired-length receives a weight of 1 and all others are assigned a value equal to their fractional length with respect to the longest. The cross-azimuth extrema are processed likewise and, then, summed with the cross-range normalized values for the final score. For the third scoring function, the scale of 0-1 corresponds to the gradient magnitude scale of highest (least important) to lowest (most important). Figure 19 shows the results from the combined interest from these three functions. Cells are coded as in Figure 18. It shows that 87.5% of the BWER ridge cells were selected by this MI approach. These selected cells accounted for 28.5% of the total identified. These results are similar to the simple MI results discussed earlier (see Table 2). Combinations of these approaches are expected to provide performance improvements and will be explored in the near future.

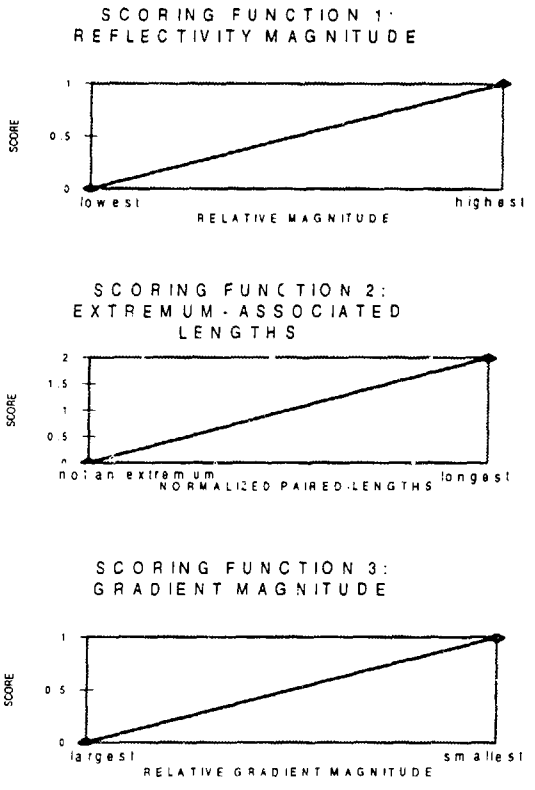

Figure 17. Three scoring functions applied without a template for a test of a third MI approach. Refer to the text for more details.

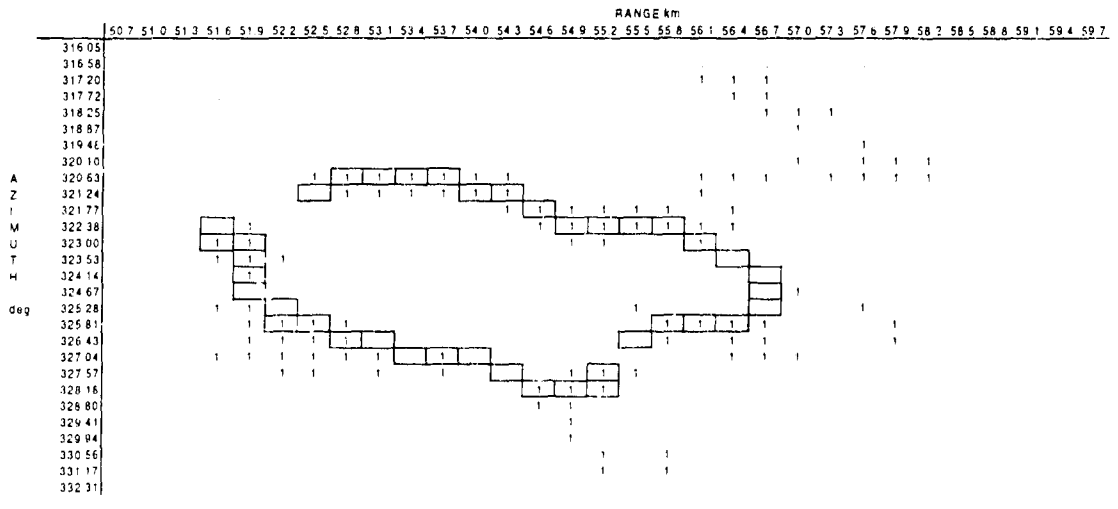

Figure 18. Results of the application of the template and scoring functions shown in Fig. 16 to the Control BWER. Cells denoted "1" were accepted after thresholding. Boxed cells reference the BWER ridge. Compare these results with those of Figs. 9 and 11. See text for more discussion.

2.6.2. Segment Building

Instead of more sophisticated MI schemes, an alternative approach is to use the additional information related to BWERs as aids in segment building. Since most of the BWER ridge points are identified as extrema, the segment joining process attempts to connect neighboring extrema in a logical way. In this way, the BWER points would be more likely than other, non-organized extrema to be joined from start to end. With the simple combined MI results as a starting point, the additional MI parameters would serve as steering or selection agents in this joining process.

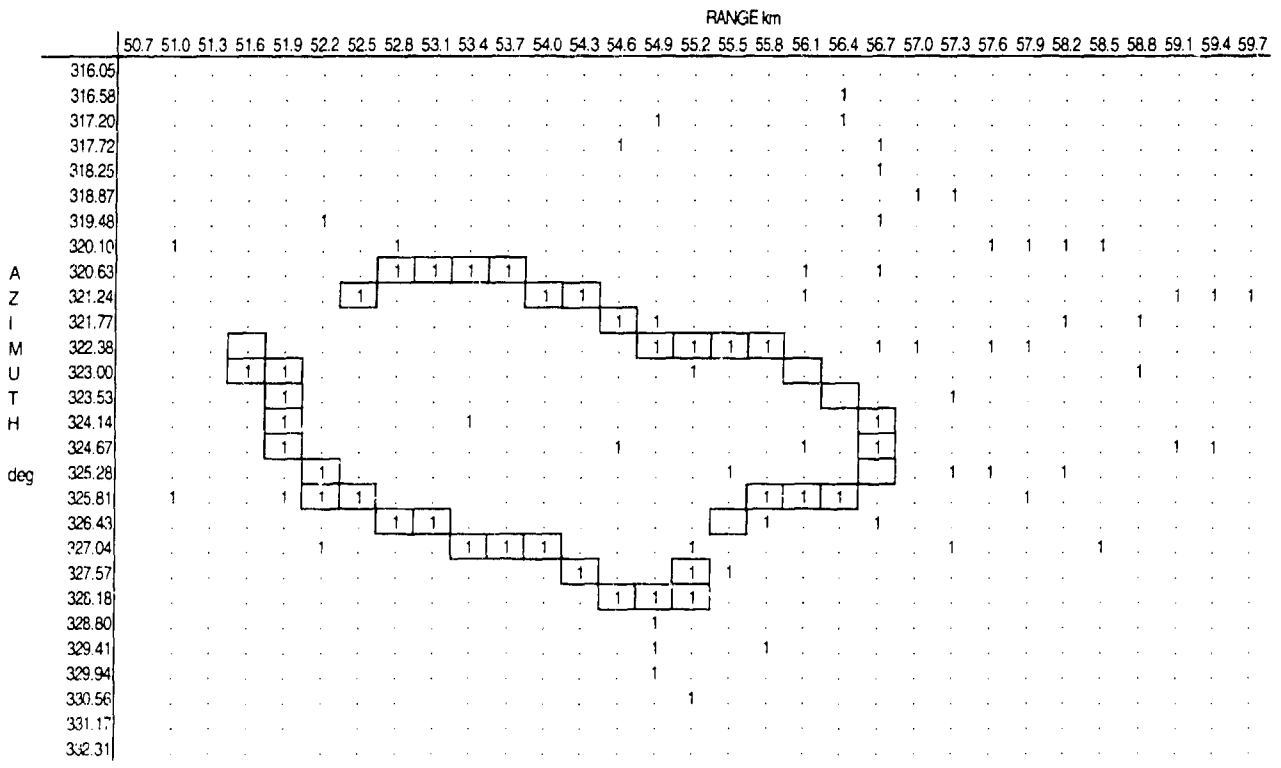

Figure 19. Results of the application of the scoring functions shown in Fig. 18 to the Control BWER. Cells denoted "1" were accepted after thresholding. Boxed cells reference the BWER ridge. Compare these results with those of Figs. 9, 11, and 17. See text for more discussion.

The procedure would be driven by the type of extremum encountered. Figure 20 helps illustrate the segment joining based on extremum type. The idea is to build an outline of the BWER along its peak reflectivity ridge. A cross range extremum indicates that the gradient ridge would lie across the radials. A cross azimuth extremum indicates the detected gradient ridge lies along the radial. Thus, the type of extremum encountered dictates the direction to search for the next extremum. If a dual type were found indicating gradients identified by both SWV methods, a

EXTREMUM TYPE

R = cross range type extremum

A = cross azimuth type extremum

D = dual type extremum

SAMPLE EXTREMA SEQUENCE

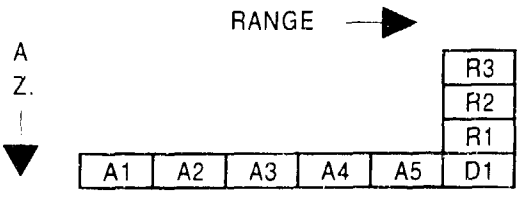

STEP	EXTREMUM	SEARCH DIRECTION	RESULT
1	A1	look left	no join
2	A1	look right	join to A2
3	A2	look right	join to A3
4	A3	look right	join to A4
5	A4	look right	join to A5
6	A5	look right	join to D1
7	D1	look right	no join
8	D1	switch directions, look down	no join
9	D1	look up	join to R1
10	R1	look up	join to R2
11	R2	look up	join to R3
12	R3	look up	segment terminated

Figure 20. Example of segment building by joining extrema. The type of extremum dictates the direction of search.

connection is first attempted in the last direction tried. If no connection is made, then the search is tried in the orthogonal sense. A non-extremum cell concludes building of the current segment.

For the Control BWER, the entire outline is not depicted with extrema. In some cases, two segments along the same range or radial are separated by a one cell gap. The segment joining process is expanded to handle this situation and is illustrated in Figure 21. This means if an extremum is not found, the segment is continued in a straight line across the resultant gap if a connection is made to another extremum.

This expansion of the simple connection method needs further augmentation for non-straight line connections.. The simple straight line segment building concept is enhanced by using directional fanning. That is, the search extends to the cell in

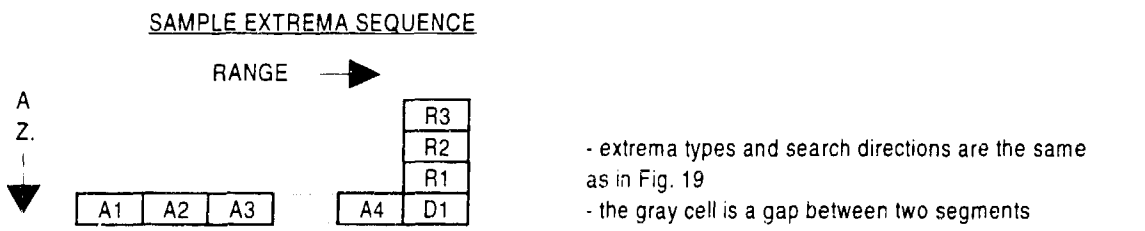

STEP	EXTREMUM	SEARCH DIRECTION	RESULT
1	A1	look left	no join
2	A1	look right	join to A2
3	A2	look right	join to A3
4	A3	look right	no join, cell reserved for potential gap fill
5	A4	look left	reserved cell encountered, join A3 to A4 via reserved cell
6	A4	look right	join to D1
7	D1	look right	no join
8	D1	switch directions, look down	no join
9	D1	look up	join to R1
10	R1	look up	join to R2
11	R2	look up	join to R3
12	R3	look up	segment terminated

Figure 21. Example of segment building with one cell gaps by joining extrema. The type of extremum dictates the direction of search.

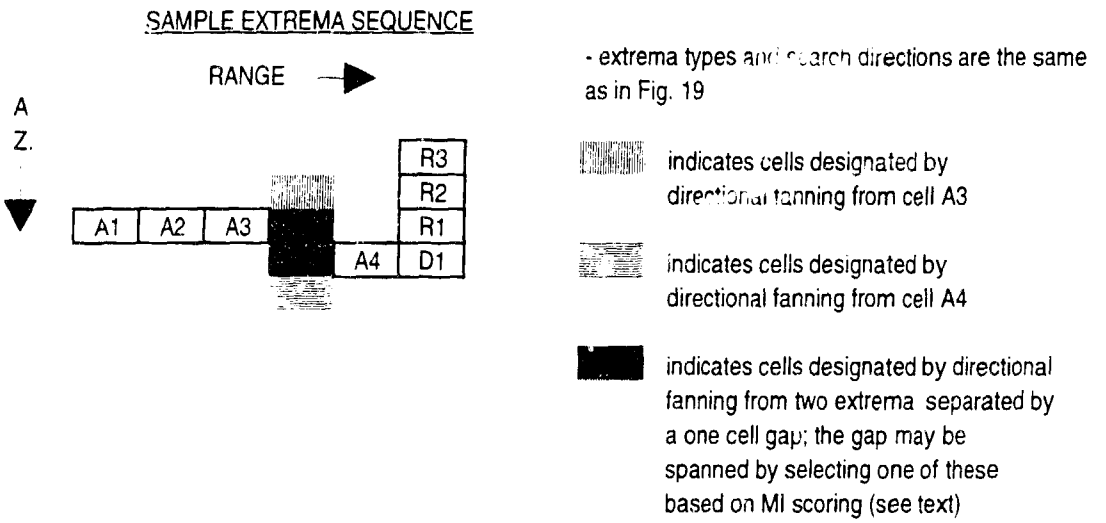

Figure 22. Example of segment building with directional fanning to make connections across gaps that are not in line. Refer to the text for an explanation of how MI parameters are used in this process.

the direction of the segment, as in Figure 20, and now also to the two cells on either side. If an extremum cell is not encountered, the segment is continued from the last extremum of the segment if any cells of a three cell fan in the search direction connect to an extremum or a fanned cell from another extremum.

It is at this point that many complicated situations arise. Refer to Figure 22. Here the gap separating the extrema has two fan overlap choices. To select only one, additional information is used; for example, magnitude, gradient magnitude, and gradient direction. Thus, the cell that has the optimal combination of high reflectivity, low gradient magnitude, and preferred directional orientation is selected. The exact combination of weights for these parameters is under consideration.

This method successfully navigates about the entire Control BWER. Depending on the actual weights used, either of the two different boundaries for the right side of this BWER are indicated. A further expansion of this technique would be to select the "best" cell of the three fanned cells if they did not join to anything. It can be imagined that two-cell gaps could possibly be closed by second-pass joining of fan-extended pseudo-extrema.

2.6.3. BWER Quantification

The purpose of identifying the BWER outline is to use it to quantify the BWER. Besides the physical characteristics of the BWER, the reflectivity and its relation to water mass are to be examined. Both 2-D and 3-D computations of the appropriate parameters will be explored. Current research focuses on detailing the shape of identified BWERs in two dimensions.

There are many ways to describe an identified feature using pattern recognition techniques. Perimeter, area, compactness, major and minor axes are some of them. Up to this point, all processing has been performed in a dimensionless two-dimensional array. For the purposes of quantification, true physical coordinates are used. Segment lengths between each cell using the coordinate positions are computed. Perimeter is simply taken as the sum of the lengths of the individual line segments comprising the BWER outline. Area is estimated by summing the area of individual trapezoidal strips created across the radials equally spaced by the range gates. To do this, the coordinates of the four corners are needed.

A computationally less burdensome approach to area estimation was also reviewed. The trapezoidal rule yields area by summing the distances across equi-spaced strips applying half weights to the two end strips. Half of this sum is multiplied by the equal spacing of the strips. This method works nicely with the equally spaced range gates. The strip distances are compared to that found in polar coordinates and found to agree within 0.38%. For the Control BWER, a perimeter of 19.34 km and an area of 18.38 km^2 were computed. The area is identical to that from summing the individual strips.

Compactness (the quotient of the square of the perimeter and area) is another measure of shape. Certain shapes such as circles, squares, equilateral triangles, and Pythagorean triangles have constant values of compactness regardless of their physical size. For constant area, as the feature becomes elongated, the compactness increases. In nature, it should be assumed that an infinite variety of shapes can occur. It is possible for compactness to approach or mimic values for standard shapes. The Control BWER compactness of 20.36 is

near the constant for an equilateral triangle. However, it has an elliptical appearance and a compactness about that of a 2.9:1 ellipse. The usefulness of this parameter is not clear at this time but is available as an option.

2.6.4. Convolution Masks

The field of pattern recognition is a large discipline beyond the Sobel operator. There are many convolution masks noted in the literature that perform a variety of functions on an array of data as was done with the Sobel operator. A variety of smoothing masks were tried early on and found to make detection of the all important gradients more difficult. Another mask for deblurring (Nadler and Smith, 1993) was tried with inconclusive results. This mask is meant to sharpen features in an image and may have limited applicability since the Control BWER extrema (i.e., outline) comprise only about 18% of the total found in the image. This may not be sufficiently robust for the deblurring mask to be effective.

Also susceptible to noise is the Laplacian mask (Nadler and Smith, 1993). As the name implies it is an operator that calculates the second derivative about a target cell. Thus, it achieves a zero value at gradient peaks and large values at the critical (or extrema) points. The Laplacian would require a filtering threshold to find the extrema, whereas the PV method does not. Additionally, directional information related to extremum type for segment building would not be readily available. It appears that this mask can add little to the information that has already been derived from alternative means. Since the final solution has not been reached, final judgment of its usefulness has been reserved for the future.

2.7. Summary

Progress has been made into the BWER identification portion of an eventual Severe Storm Structure algorithm. The algorithm is intended to aid in distinguishing the likelihood and intensity of severe weather in supercell thunderstorms. These storms are driven by intense, organized, long-lived updrafts. On a radar reflectivity PPI, the BWER is a primary feature indicative of storm updraft intensity. The development of identification techniques has focused initially on that feature. We

think that these techniques will be applicable to the identification of other features, particularly the WER. The idea has been to use pattern recognition of features in B-scan versions of the data and to convert feature positions to Cartesian or spherical coordinates only if required for quantification purposes.

Relying on the salient reflectivity features of the BWER, we have developed clear steps towards identifying the BWER border even in the presence of spurious features. Old (pattern vectors) and new (machine intelligence) methods have been combined to identify features while minimizing computational load. Early results indicate that these techniques should be applicable to WERs. This phase of the algorithm development has advanced to the point where initial inspection of the quantification issues is warranted.

The immediate tasks are to finalize this first version of the identification portion of the algorithm and develop, modify, and test the quantification schemes. As the algorithm stands now, the following processing steps have been adopted:

a. acquire single scan radar data,

b. distinguish individual storms,

c. eliminate spurious data for each storm,

d. identify the region of highest reflectivity,

e. process this region for extrema via pattern vectors,

f. using MI principles, retrieve parameters such as gradients,

g. combine these parameters to identify the BWER,

h. quantify the BWER,

i. relate to severe weather occurrence and type.

3. LIGHTNING PREDICTION IN AIR MASS THUNDERSTORMS

3.1. Introduction

For convective storms developing in a weakly sheared environment, considerable evidence has been amassed that relates radar reflectivity structure and lightning activity. Marshall and Radhakant (1978) suggest that the electrical activity of thunderstorms is related to radar reflectivity observed at the 6 to 7 km level. This idea was further tested by Lhermitte and Krehbiel (1979). They horizontally integrated the radar reflectivity of a storm at several heights and found that intra-cloud (IC) lightning began when the storm top reached 8 km (-20°C). Also, they found that the peak flash rate (about 1 flash/s) occurred when the reflectivity exceeded 50 dBZ at the -10°C level. Buechler and Goodman (1991) observed that cloud-to-ground (CG) strikes began when the reflectivity values of 30 - 40 dBZ extended above 7 km. While all the above observations were made in Florida, similar altitude or temperature thresholds were found in New Mexico (Krehbiel, 1986) and the tropics (Williams, 1991). Other studies have looked at various methods of comparing reflectivity data and lightning activity. A recent study by Harris-Hobbs et al. (1992) attempted to correlate lightning activity with storm volumes exceeding various thresholds. They found good correlations between the volume exceeding 20 dBZ and flash activity. However, for some of their data, regions with even higher reflectivity thresholds attain peak volumes before either lightning activity or the region within the 20 dBZ contour has maximized. While this suggests another prediction tool, it should be noted that most other observations indicate that lightning activity is directly proportional to the storm mass. It should be apparent that many workers have found relationships between reflectivity and the onset of lightning activity. However, no clear criteria have been established because most of the conclusions have been based on limited case studies. With routine data collections from NEXRAD systems, more definitive criteria should now be possible.

Another recent study (Holle et al., 1992) has provided an evaluation of the predictive potential of the surface convergence for lightning activity. Their study was

based on convergence estimates with a network of surface stations. They found the probability of detection was about 60% but false alarm rates were of the same order or higher. These results are not as good as those obtained by Watson et al. (1991) who had a more dense network of stations. This dependency upon network density is not surprising since the convective storms tend to be comparable to or smaller than the network resolution. Therefore, the enhanced resolution of Doppler weather radar should provide even better correlations. Holle et al. attempted to evaluate the use of Doppler data but were limited by vertical resolution of the data and the limited scope of their analysis. The gradient technique developed by **HSTX** should provide better and more complete detection of the boundary layer convergence. While this is not a primary goal of the research in this proposal, attempts will be made to evaluate the use of radar in the detection of boundary layer convergence.

3.2. Microphysical Characteristics

In convective storms charge separation occurs resulting in regions with excess positive and negative charges. Lightning is the process of equalizing these charges by producing a negative current flow from the excess negative charged region to the excess positive charge region, or vice versa. Because air is a poor conductor, the electric potential between these charged regions must be very high, about 3000 volts/m. According to Mason (1971) the most likely mechanisms for charge generation and separation in thunderstorms are the fragmentation of droplets impacting and freezing on hail pellets and the rebound of ice crystals or cloud drops from hail in polarizing electric fields. Both of these mechanisms have the effect of imparting a negative charge to the hail and an equal positive charge to the shed or rebound cloud particle. The cloud particles remain aloft, while the hail falls. This gives the often observed structure of positive charge in the uppermost portions of the cloud with negative charges in the lower portions. A corresponding enhanced positive charge develops beneath the cloud and a lightning discharge occurs between the ground and the cloud base. At least this is the commonly quoted configuration in texts (e.g., Lutgens and Tarbuck, 1979). From this configuration, one would expect the greatest negative charge buildup to be where the most and largest hail is located and that the lightning would emanate from there. This would

be from the high reflectivity regions. However, recent correlations of the occurrence of lightning with radar reflectivity indicates that while lightning frequency is the greatest when the integrated storm mass is the greatest, the lightning itself is not directly associated with the maximum reflectivity. Instead, it usually occurs in regions of little or no reflectivity at low altitudes and near large horizontal gradients of reflectivity around the main reflectivity core (e.g., Lopez, et al., 1989; Nielsen and McGorman, 1989; Watson, et al., 1989). While a very large percentage of lightning occurs near the reflectivity core, there is considerable activity that occurs in the anvil, at significant distances from the core. Ziegler et al. (1986) observed significant activity between the -40°C level and the ground in regions of weak convective activity. They also noted that much of this activity was associated with the anvil region. Rutledge et al. (1991) observed significant lightning activity in stratiform precipitation associated with convective storms.

3.3. Storm Structure Characteristics

There have been many studies that have related storm structure to the onset of lightning. Most of these studies revolve around the relationship between cloud top height and the height of some isotherm. For example, Dye et al. (1989) found that in New Mexico storms significant electrification occurred only with radar reflectivities above 40 dBZ at the -10°C level and cloud tops above the -20°C level. Lightning occurred only when tops extended above the -25°C level. Saunders (1993) notes this observation by Dye et al. is consistent with conclusions drawn by Reynolds and Brook (1956).

Many researchers have pointed to an association of lightning activity with vigorous convection, as evidenced by radar measurements of reflectivity and echo top height. One of the earliest studies of this association was conducted for New England thunderstorms by Shackford (1960). Lopez et al. (1989) showed the evolution of peak reflectivity and lightning strike rates to ground in a couple of Colorado storms, and it appears that there was no lightning until reflectivities exceeded about 30 dBZ. Buechler et al. (1990) observed in one storm in Tennessee that 30 dBZ echo appeared in the storm about 20 to 25 minutes before lightning

activity. In Florida, Beuchler and Goodman (1991) found, in a preliminary study of only three storms, that extension of 30-40 dBZ reflectivity above 7 km (or -10°C) precedes cloud-to-ground lightning. Shchukin et al. (1993) studied electrically active storms in the vicinity of St. Petersburg, Russia and found that, generally, initial lightning discharges await growth of radar reflectivity to its maximum at a height of 2 - 3 km above the 0°C level. Weber et al. (1993) discuss a couple of Florida event wherein the growth of the 20 dBZ echo top to well above the 0°C level preceded the first intracloud lightning by several minutes and the first ground strikes, in one case, by an additional 12 minutes. Petersen et al. (1993) show that echo centroid height above 0°C level is a much better indicator of electrification than echo top, in TOGA-COARE observations in western equatorial Pacific. However, they define echo centroid as reflectivities equal to or greater than 25 dBZ, which is simply a thresholded echo top and has the distinct advantage of amenability for objective measurement.

Polarimetric radar may reveal characteristics of particles in the mixed phase region of convection where electrical charge may be generated. Goodman et al. (1989), encouraged by investigations by Seliga et al. (1986) and Illingworth et al. (1987), studied the electrical history and nature of precipitation two storms that produced downbursts. Goodman and Raghavan (1993) continued use of a polarimetric radar as well as some other novel sensors, to study a rather lively thunderstorm near Cape Canaveral, Florida, using data from the CaPE experiment. More polarimetric studies of CaPE storms were reported by Bringi et al. (1993a,b), Detwiler et al. (1993), and Breed (1993). A good explanation of ZDR (differential reflectivity) at S-band and LDR (linear depolarization ratio) at X-band was presented by Breed, with a tip of the cap to the pedagogic skills of Herzegh and Jameson (1992). Above the 0°C level, the higher ZDR values indicate supercooled liquid raindrops sufficiently massive to take on an oblate spheroidal shape. On the other hand, large LDR values indicate transition regions of wet growing graupel or frozen drops.

An important part of this study will be the verification of lightning occurrence. This can best be accomplished through VHF interferometry, from which images of

lightning strokes can be generated so that intra-cloud flashes can be distinguished from cloud-to-ground strikes. Richard (1990,1991) presents an informative overview of the SAFIR interferometry system. He notes that intra-cloud lightning leads cloud-to-ground lightning by 5 to 30 minutes. This means that this system can provide some lead time for the initiation of cloud-to-ground lightning. The SAFIR system has been used in Orlando, Florida (Laroche et al., 1991 and Weber et al., 1993) and near Paris, France (Jucanon du Vachat and Cheze, 1993).

3.4. Storm Precursors

Another approach reaches back in time for determination of antecedent conditions favorable for convection, by searching for convergent lines (or zones) in the boundary layer as precursors of convection. Purdom (1973) was the lone and often embattled pioneer in calling attention to the importance for subsequent thunderstorm of two boundaries visible in satellite imagery. Intersection of the two boundaries is particularly important. Donaldson and Burgess (1982) discussed an explosive tornado outbreak in Oklahoma, along a locus of intersection of a cold front overtaking a dry line. The National Center for Atmospheric Research (NCAR) has been extremely active in the study of boundary layer convergent lines. Wilson and Carbone (1984) proposed the study of even cloudless lines using sensitive Doppler radar. Wilson and Schreiber (1986) showed a radar-detectable boundary antecedent for the vast majority of thunderstorms in central Colorado. Wilson and Mueller (1993) attempted 30-minute nowcasts of thunderstorms, based primarily on Doppler radar observations of clear-air boundaries, as well as subsequent visual sightings of clouds and radar measurements in developing storms. There seemed to be some skill displayed in predicting initiation. They think they will do better after they implement an automated boundary detection scheme developed by Rogers et al. (1991). Eilts et al. (1991) have their own "gust front detection algorithm" for the vicinity of Orlando, Florida; they feel that an echo aloft of 10 dBZ or more appearing above a boundary layer convergence zone precedes the first lightning strike by 8 to 21 minutes. Keenan et al. (1992) have also demonstrated success in storm forecasts in the Darwin, Australia region, based primarily on Doppler radar detection of convergent boundaries. Incidentally, Wilson et al. (1993) have made a very

convincing case, using multiparameter and multiwavelength radar in both Florida and Colorado, that the thin boundary layer convergent lines do indeed mark the location of updrafts. They show that the boundary echoes are returns from particulate scattering, and the scatterers, similar to flying insects, have a distinctive long axis oriented horizontally. Further, Achtemeier (1991) has found that insects resist being carried aloft to colder temperatures, so in an updraft their concentration will increase, thereby enhancing markedly the reflectivity of the convergent boundary.

3.5. Candidate Parameters

Two distinct approaches appear to have promise:

- detection of convergence lines in the boundary layer
- detection of moderate values of reflectivity at altitudes a kilometer or more above the 0°C level.

As the many investigations of Wilson and his colleagues show, boundary layer convergent lines are strongly implicated as an indicator of the earliest stages of convection. Because their studies were conducted only in Colorado and Florida, the generality of their findings must be verified. This requires statistical studies by region. In addition, quantization is required to determine the value of such lines for the prediction of sufficient convection of lightning to be produced. This predictive value could be a function of line intensity, as measured by convergence, reflectivity, and a "lineness" structure function. Detection of convergence lines would yield the greatest lead times before lightning strikes but would be prone to high false alarm rates.

To detect the convergence lines we will use the techniques being developed to assess frontal structure, described in the next task. That technique computes the two-dimensional gradient of the Doppler velocity and extracts lines of maximum gradient. This is exactly the type of detection needed for this task. We will then correlate these lines with lightning occurrence.

The other promising approach is to catch the process of convection at a stage where electrification can proceed. There would be less warning lead times with this approach, but the field of possible candidate lightning producers would be narrowed. This would reduce the false alarm rate and provide more precision in location of the threat. Most studies to date require reflectivity to exceed a somewhat arbitrary threshold value at a specified height above the 0°C level. Rather than focus on point values of reflectivity, we favor an integrative solution. Also, it appears to be useful to examine the spatial and temporal gradients of reflectivity.

For reflectivity monitoring we will use some of the techniques outlined in the previous task on Severe Storm Structure. This task will involve the monitoring of locations and magnitudes of significant gradients, the areas and volumes within specified reflectivity contours, and maximum height and centroid computations.

4. FRONTAL STRUCTURE

4.1. Introduction

The purpose of this task is to develop an algorithm based on Doppler radar data to study the three-dimensional structure of fronts as a function of time. This task will involve four distinct phases:

- Front detection
- Two-dimensional structure definition
- Three-dimensional structure definition
- Establishment of relationships of changes in structures to meteorology.

By monitoring the changes in the structures of fronts, we anticipate that forecasts of associated meteorological events such as wind shear and precipitation can be improved. This report addresses efforts directed toward the first phase, front detection. In this phase, we compute the basic fields to be used throughout the algorithm and develop a front detection scheme based on those fields that will serve as a means of focusing further data processing.

4.2. Algorithm Development

4.2.1. Fronts in Radar Images

Fronts are the source of many weather events that produce a wide variety of weather activity. Baroclinic instability in the atmosphere leads to the formation of synoptic scale fronts and to the formation of smaller scale cyclones along the fronts. Fronts are regions of transition in the temperature and wind fields. They always occur in pressure troughs where there is enhanced vorticity. Strong fronts will have significant vorticity and convergence. Variations in frontal strength will be reflected in both of those fields. An increase in the horizontal gradient of an air mass property, such as temperature and/or humidity, and development of convergence and curvature indicate the formation of a front (frontogenesis). A decrease in horizontal gradient of the air mass properties and the dissipation of the accompanying wind structure field indicate the dissipation of a front (frontolysis).

On a radar display, fronts are often identified by regions of sharp gradients in the radial velocity field and sometimes by thin lines in the reflectivity fields. Doppler radar provides reflectivity and radial velocity data and gives indications of precipitation location, precipitation intensity, and air flow. NEXRAD (Next Generation Weather Radar) is a network of Doppler radars with sophisticated processors for rapid data processing that is currently being deployed. These radars have vastly improved sensitivity and processing over the WSR-57 systems that they are replacing. As a result, this network will provide better definition of weather structures, rapid location of severe weather activities, and more consistent monitoring of intensity trends.

Weather radar is effective to ranges of 200 to 400 km. It is, therefore, an important tool for mesoscale meteorology, especially for the observation of frontal structure. It provides a way to tie precipitation patterns or convective activities to synoptic scale cyclones and fronts. Early radar work showed the broad, diffuse echoes associated with warm fronts and the discrete, intense cells that accompany

some cold fronts. Also, radars have detected intense thunderstorms near warm fronts, bands of convective cells in the warm sectors of frontal cyclones, and fronts devoid of precipitation.

As noted above, gradients are an important feature associated with fronts. A major focus of our work will be the quantification and characterization of these gradient fields. In the WSR-88D algorithm inventory, the Combined Shear algorithm provides products that could be used for this purpose. However, that algorithm is very inefficient and consumes considerable computer resources. In the previous contract, a more efficient gradient technique based in the rectangular Cartesian coordinate system was developed and applied to the detection of edges of meteorological features (Hamann, 1991). However, even this technique is relatively slow and cumbersome because it requires intermediate interpolation and a time-consuming search procedure. Under the current contract, the computation of gradients in polar coordinates is addressed. Furthermore, alternative schemes of feature extraction are studied for more efficient processing.

4.2.2. The Front Detection Technique

Algorithms have been implemented to detect fronts and to study frontal structure. The techniques are based in a two-dimensional polar coordinate domain, with processing performed on each constant elevation angle plane in which the radar data are collected. The intent of this work is to incorporate the results from all elevations into a three-dimensional structure that is then evaluated with time. In this report only the two-dimensional front detection in polar coordinates will be discussed. Processing steps involve preprocessing of input images, edge detection of gradient discontinuities, and feature extraction of frontal boundaries.

4.2.2.1. Preprocessing of Input Image

Data quality is very important for algorithm development. Clutter contamination, random noise, missing data, and velocity-folded echoes can create

extensive problems for the radar user. Preprocessing, a set of procedures that mitigates ambiguities in the data, is a requirement for the best performance of any algorithm.

4.2.2.1.1. Noise Filtering

Radar images are not perfect; they always contain noise and missing data. To assess the noisiness of the data, each data point is checked for consistency with its neighbor. Two approaches have been addressed: the four-cross-points filter and the eight-points filter. In both approaches, only missing or noisy data are replaced by average values. The level of noise was determined by comparing each data point to the mean of four cross points or eight surrounding points. A data value is designated as noise if the difference between it and the mean of the surrounding points exceeds a threshold value. When these schemes were applied to the reflectivity and velocity fields, the resultant fields for the four-cross-points filter were noisier than for the eight-points filter. In both approaches, the process improved the continuity of the gradient field and helped the process for edge detection and feature extraction. All small areas of missing and noisy data were replaced with average values.

4.2.2.1.2. Velocity Dealiasing

Velocity aliasing is often a major concern in radar data processing. The aliasing not only produces misrepresented velocities, but also results in artificially enhanced velocity gradients. All data used in this study have been dealiased with a simple technique based on pattern recognition techniques. This technique will be described in a future report.

4.2.2.2.Gradient Computation

Experiments with human vision have shown that gray-level contrasts or boundaries in images are very important in the recognition of objects. Hubel and Wiesel (1979) suggest that the visual systems of mammals respond to edges of

images. This response can be simulated by employing template - matching edge operators. A template - matching edge operator is a mathematical operator with a small spatial extent designed to detect the presence of a local edge within an image. The gradient operator is the most common edge operator to be used to extract boundaries of image objects. We have adopted this operator as an edge detector to determine the frontal boundary. The direction of the gradient vector is aligned with the direction of maximum gray-level change, and the magnitude is an indication of the intensity of this change.

The gradient for an image function $f(r,\theta)$ in polar coordinate space (r,θ) can be expressed in a total derivative form as

$$f(r,\theta) = (\partial f(r,\theta)/\partial r , \partial f(r,\theta)/\partial \theta * \partial \theta/\partial s) \text{ where, } \partial \theta/\partial s = 1/r$$

In practice, the gradient computation can be accomplished through a convolution operation. The center of the spatial difference operator is placed on a point in the image. A pair of templates at orthogonal orientations is applied in the polar coordinate plane (Figure 23). This convolution operation produces estimates of the local gradient vector at each image point. The template size can be varied with image resolution. As the image resolution becomes coarser, gradients decrease and object boundaries converge and become less distinct. The template size should be minimized to detect edges effectively.

The gradient is a vector that gives the direction of the most rapid change of field, and the magnitude of this vector gives the rate of change in that direction at point (r,θ). In digital images the components are obtained by finite difference operations on small windows. The local gradient magnitude (G) and direction (ϕ) can be computed from the difference operators along the directions (1 and 2) as

$$G = (\Delta_1^2 + \Delta_2^2)^{1/2}$$

$$(1)\ \begin{vmatrix} -1 & -1 & -1 \\ 0 & 0 & 0 \\ 1 & 1 & 1 \end{vmatrix} \quad \begin{vmatrix} -1 & 0 & 1 \\ -1 & 0 & 1 \\ -1 & 0 & 1 \end{vmatrix} \qquad (2)\ \begin{vmatrix} -1 & -1 & -1 & -1 & -1 \\ -1 & -1 & -1 & -1 & -1 \\ 0 & 0 & 0 & 0 & 0 \\ 1 & 1 & 1 & 1 & 1 \\ 1 & 1 & 1 & 1 & 1 \end{vmatrix} \quad \begin{vmatrix} -1 & -1 & 0 & 1 & 1 \\ -1 & -1 & 0 & 1 & 1 \\ -1 & -1 & 0 & 1 & 1 \\ -1 & -1 & 0 & 1 & 1 \\ -1 & -1 & 0 & 1 & 1 \end{vmatrix}$$

Figure 23 . Examples of gradient templates: (1) 3x3, (2) 5x5

$$\phi = \tan^{-1} (\Delta_2 / \Delta_1)$$

where, $\Delta_1 \sim \partial f(r,\theta)/\partial r$

$$\Delta_2 \sim \partial f(r,\theta)/\partial\theta * \partial\theta/\partial s$$

In the computation, the radar field is presented in matrix notation. The ranges (r) along the radial beam are treated as columns. The azimuth angles (θ) are treated as rows. The pair of templates depicted in Figure 23 are applied. The magnitude of the local total derivatives and corresponding gradient directions are computed. The calculated edge values are small for smooth images and large for discontinuous images. The detected edges are later used in feature extraction.

4.2.2 3.Front Extraction

A frontal feature is often associated with a convergence line in the velocity field and an enhanced reflectivity line in the reflectivity field (Wilson and Schreiber, 1986). Theoretically, the edges in the reflectivity gradient field correspond to the enhanced reflectivity line and the edges in the velocity gradient field correspond to the convergence line. The front feature can be then identified. Unfortunately, the world of image processing is not always straight forward. There is always some uncertainty as to which local edges correspond to the front.

Three feature extraction schemes were implemented to determine the frontal boundary. These include the modified heuristic search procedure, the thresholding scheme, and the Hough transform scheme. Each will be discussed in detail.

4.2.2.3.1. Modified Heuristic Search Procedure

This scheme is modified from the one developed in the previous contract (Hamann, 1991). In our new scheme, the gradient vectors are computed in polar coordinates and sorted according to magnitude. The search procedure starts with the strongest gradient. From that point, a boundary line is constructed by bilaterally utilizing adjacent strong gradients with consistent directions. Once a line is complete (i.e., cannot be extended further), the procedures are repeated by searching all remaining gradient vectors. The results are arrays of line segments. The shorter segments are eliminated by length thresholding. For the front, the end result is generally a set of broken lines aligned along the frontal position. This entire scheme is a very time-consuming procedure.

4.2.2.3.2. Thresholding Scheme

A binary field is created by thresholding. In this process, the data values less than or equal to a given threshold value are set to zero and all greater than the threshold are set to one. For front extraction, we use the gradient magnitude fields. The magnitudes are sorted in descending order. A threshold value is applied so that the largest gradient values are used. The threshold can be varied, depending on the level of detail desired for edge extraction. The entire field is processed at one time by thresholding on magnitude and requiring gradient directions for adjacent data points to be consistent, that is, to vary only within specified limits. The qualified edges are assigned indices and stored in arrays. The shorter segments are eliminated by length thresholding with criteria similar to those for the previous scheme. Results are similar too, but processing is much faster.

4.2.2.3.3. Hough Transform Scheme

The Hough transform is an extremely useful tool for the extraction of data organization in the presence of noise. It assumes that there is an analytical function with a finite number of parameters that describes this organization and that the form of that function is known. For example, you may know (or assume) that the data are

somewhat organized along a straight line, but you do not know what the parameters are for that line. Or you could assume that the data are distributed along an arc of a circle. The Hough transform provides a convenient way to extract the parameters for any curve for a given data set. Let's look at a simple application of the Hough transform. Assume that we have a collection of data points distributed as seen in Figure 24a. The organization of these points suggests that a straight line representation might be reasonable. We can represent that straight line in terms of a slope relative to a reference axis and an orthogonal distance from a reference point. Through each data point, a large number of straight lines can be drawn, each with its own slope and orthogonal distance. When this is done for all data points, a large number of slope-distance pairings are available to construct a histogram (Figure 24c). [Note that the histogram in Figure 24c is purely fictitious and is used purely for illustration purposes.] Every point that is near or on a preferred line will have at least one value for the slope-distance that is similar to teach other and to that for the preferred line. The resultant histogram will have a peak corresponding to the slope and distance for the preferred line. This slope-distance pair can be used to construct a straight line through the data (Figure 24d).

This technique provides an extremely powerful means of extracting data organization, particularly when the following refinements are considered:

- While it can be very computationally intensive when computing the line parameters, the range of parameters can be severely restricted by using constraints based on vector gradient directions.
- Weights can be applied to the data to further enhance the detection capability.
- Other functional forms such as circles, ellipses, parabolas, etc. can be used.
- Multiple lines may be detected as multiple peaks in the histograms.

The Hough transform has been successfully applied to Doppler radar data to extract straight line segments. Its use and application will be explored during the next two years of the contract.

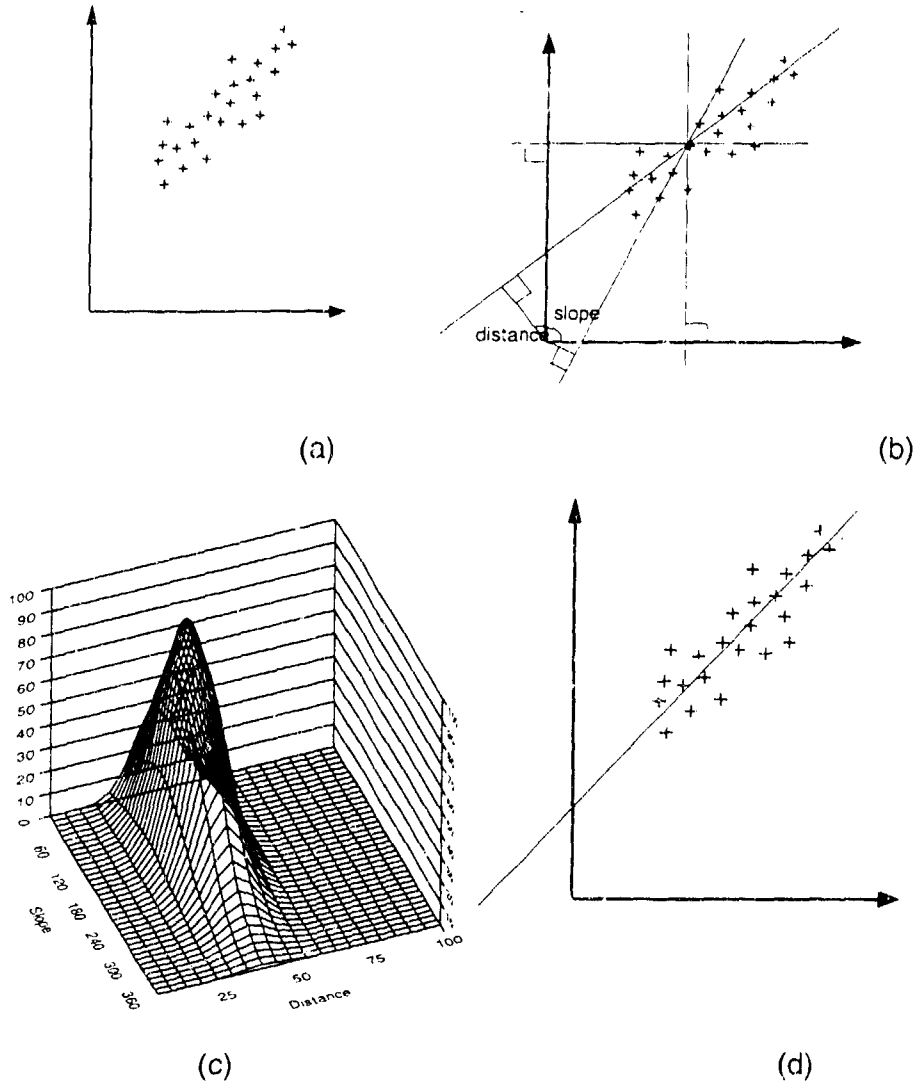

Figure 24. Hough Transform Schematic

4.2.3. Analysis

The two-dimensional polar coordinate front detection algorithm has been tested on cold front data collected by the PL Doppler radar at a low level scan at 1608 GMT 16 November 1989. The data are displayed in B-scan mode with azimuth angle as the horizontal coordinate and range as the vertical coordinate. Figure 25 depicts the original reflectivity and Doppler velocity images in various shades of gray

to indicate the optical intensities. This radar has a wavelength of 11.07 cm, beam width of 1.0°, gate spacing of 0.15 km, and maximum unambiguous velocity of 27.65 m/sec. Each gate along any given radial is considered a single point of the data field. The position of the front is located at the boundary of maximum gray-level change in Figure 25. The algorithm performance for this particular case is addressed and analyzed. The following subsections detail results from examining different ways to determine frontal position

4.2.3.1.Gradient Magnitude

The gradient magnitude is determined from computations of gradients (Δ_1 and Δ_2) in two orthogonal directions. The magnitude can then be estimated from

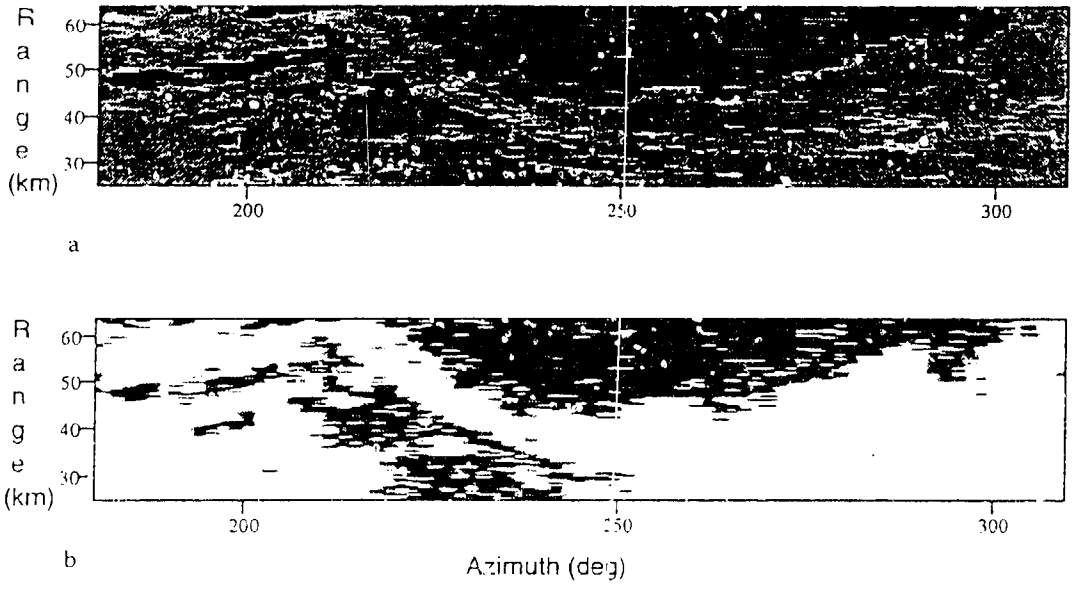

Figure 25. Original front images. (a) Reflectivity field (b) Velocity field

one of the following methods:

- compute the magnitude of the vector sum of the components
- the maximum of the absolute values of the two components
- the sum of the two values of the two components.

The first of these is obviously the most accurate but also the most computationally intensive. The others have less computational impact. Gradient components are computed using templates as previously described. Estimates of the magnitude of the gradient vector were then estimated using the three methods

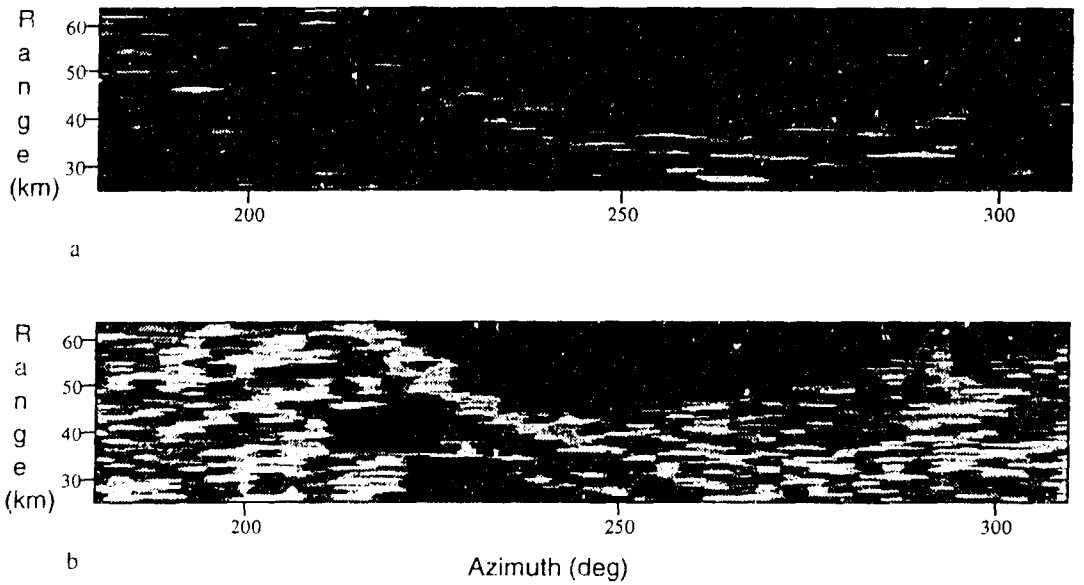

Figure 26. Edge detection for reflectivity field using a 3x3 template. (a) Gradient magnitude (b) Gradient directions

listed above. The three formulations resulted in very similar gradient estimates and virtually no variation in the resultant edges. Regardless of gradient formulation, there are always two thin edge zones along each side of enhanced reflectivity zone in the reflectivity gradient field (Figure 26a). In the velocity gradient fields, there are several broken lines above the frontal position in the velocity gradient field (Figure 27a). Both fields contain many small edge segments on the left side of Figure 26a and Figure 27a. To preserve gradient accuracy at this phase of the study, all gradient magnitude computations will use the first method, namely, vector addition.

4.2.3.2.Gradient Direction

The direction of a gradient vector indicates the direction of maximum local gray-level change. In practice, the edge operators detect a local edge where the local gradients change rapidly perpendicular to the boundary. Since the front images are noisy, the directions of detected edges are noisy (Figure 26b and Figure 27b). It is difficult to specify which local edge orientations correspond to the frontal boundary. Only those gradient magnitudes whose corresponding directions are approximately orthogonal to the frontal boundary are retained.

A thresholding technique is used to extract edges with consistent directions. In the reflectivity field, the directions of the positive maximum gray-level change associated with the front are between 240° and 330° (Figure 28a). In the velocity field, the directions of the maximum changes along the front are between 60° and 150° (Figure 28b).

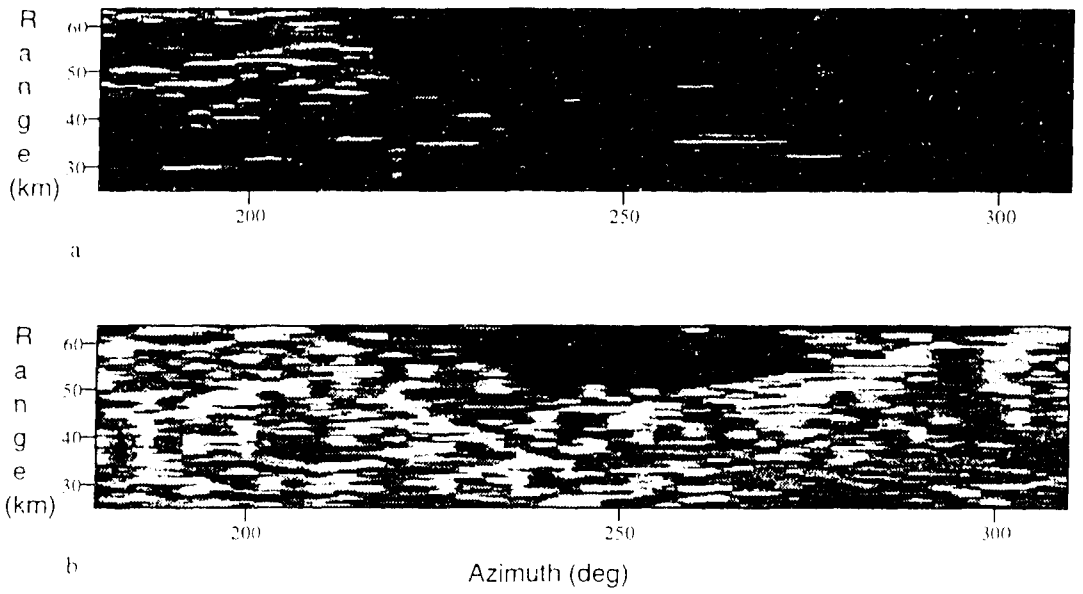

Figure 27. Edge detection for velocity field. (a) Gradient magnitude (b) Gradient directions

4.2.3.3. Operator Size

As a rule, the size of the template should be small enough so that the gradient is a good approximation to the local changes in the data, but large enough to overcome the effects of random variability. The center of the window is moved one pixel along a row or column, until the entire row or column is processed. It then moves on to the next row or column until the entire image is processed. Convolution is a linear operation. If the windows are too large, the numbers of calculations will be too large for real-time applications.

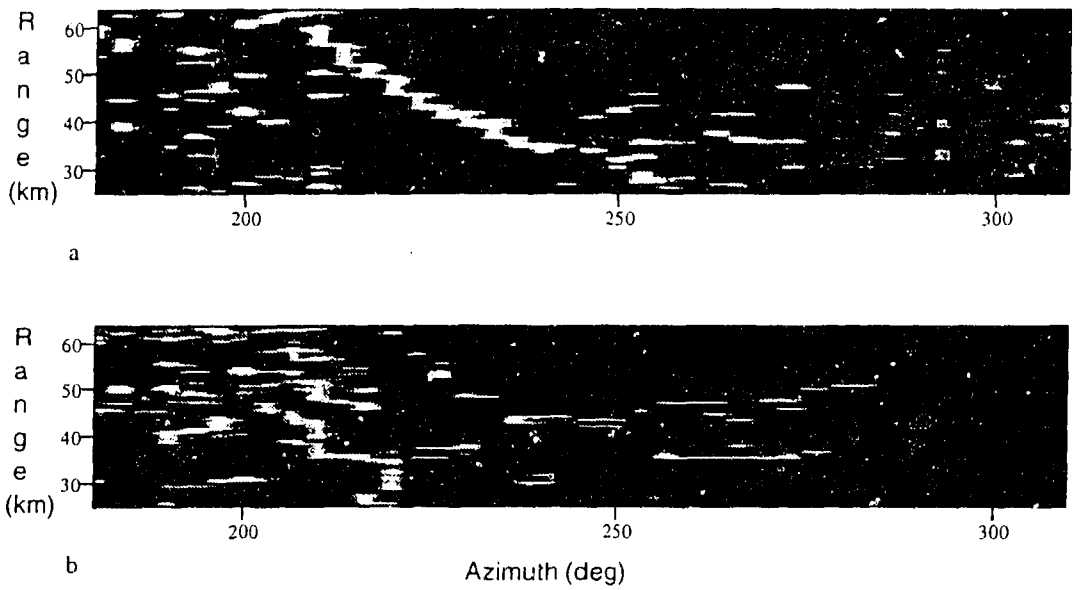

Figure 28. Gradient directions. (a) Reflectivity field (b) Velocity field

Three template sizes (3x3, 5x5, 7x7) were applied to the data. Results indicate that smaller templates produce thinner edges (Figure 29). However, small templates suffer more from noise. To minimize uncertainties from noise, operator size can be increased, which, in turn, results in smaller gaps and thicker edges. The size of the template should be tailored to the data set being analyzed. The emphasis should be on using the smallest template that yields reasonable results. For the remainder of this study, the 3x3 template will be used.

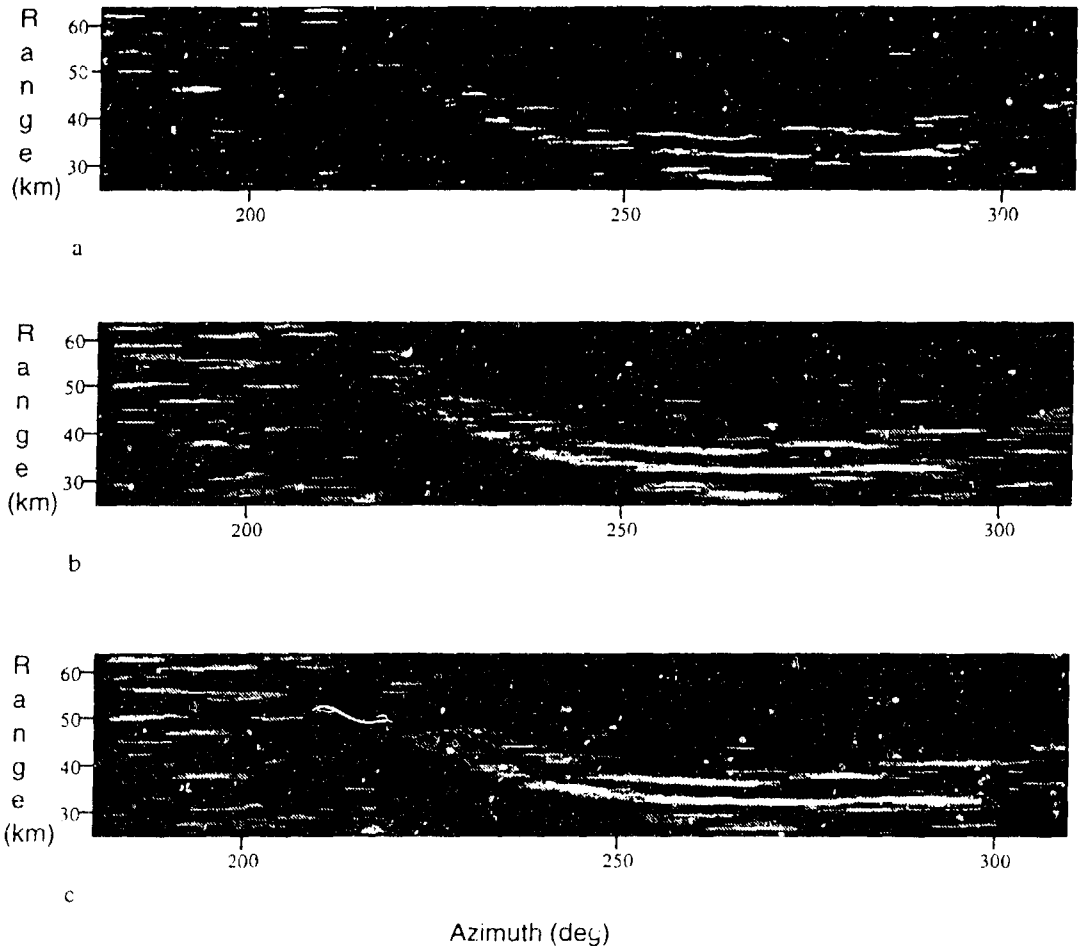

Figure 29. Edge points for reflectivity field with different operator sizes: (a) 3x3 (b) 5x5 (c) 7x7

4.2.3.4. Template Structure

Besides template size, the weight distributions within the template can be varied. Three types of 3X3 gradient operators were tested and compared (Figure 30):

- Uniform weight function with axes parallel to template axes (orthogonal operator)
- Uniform weight function with axes at 45° to the template axes (diagonal template)
- Central weighted function with axes parallel to template axes (Sobel operator)

The orthogonal and diagonal operators ((1) and (2) in Figure 30) produce very similar results. On the other hand, the Sobel operator ((3) in Figure 30) detects more gradient points than the other two operators, but it made the gradient field noisier (Figure 31). However, after the feature extraction procedure is applied, the results are similar to those derived from the other templates. The more conventional orthogonal operator is used in all further processing.

$$\begin{vmatrix} -1 & -1 & -1 \\ 0 & 0 & 0 \\ 1 & 1 & 1 \end{vmatrix} \quad \begin{vmatrix} -1 & 0 & 1 \\ -1 & 0 & 1 \\ -1 & 0 & 1 \end{vmatrix} \qquad \begin{vmatrix} -1 & -1 & 0 \\ -1 & 0 & 1 \\ 0 & 1 & 1 \end{vmatrix} \quad \begin{vmatrix} 0 & -1 & -1 \\ 1 & 0 & -1 \\ 1 & 1 & 0 \end{vmatrix} \qquad \begin{vmatrix} -1 & -2 & -1 \\ 0 & 0 & 0 \\ 1 & 2 & 1 \end{vmatrix} \quad \begin{vmatrix} -1 & 0 & 1 \\ -2 & 0 & 2 \\ -1 & 0 & 1 \end{vmatrix}$$

(1) (2) (3)

Figure 30. Three Types of Gradient Operators: (1) orthogonal, (2) diagonal, and (3) Sobel

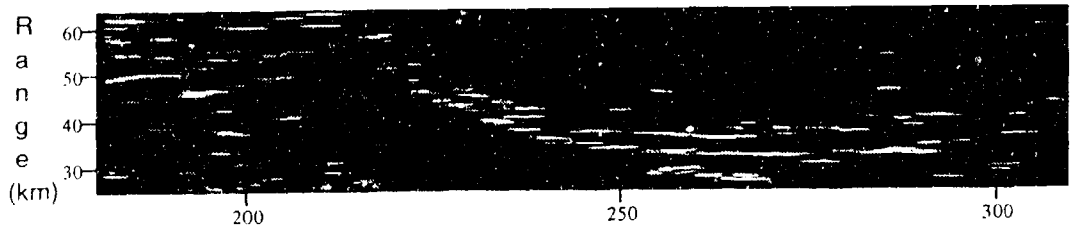

Figure 31. Edge Points on Reflectivity Field for Different Template Structures: (A) Orthogonal Operator; (B) Diagonal Operator; (C) Sobel Operator

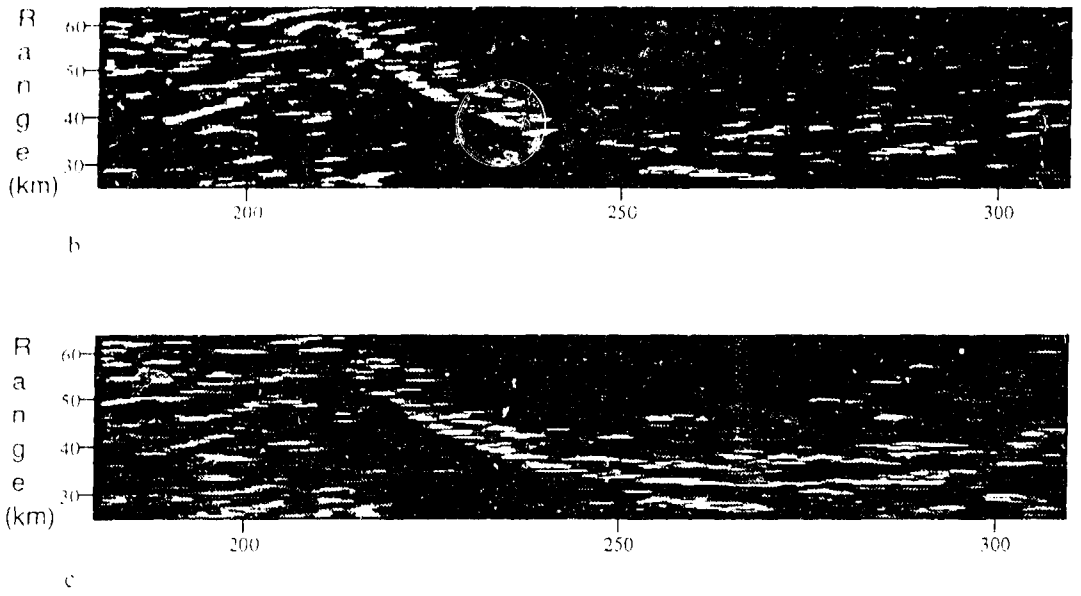

Figure 31 Continued

4.2.3.5.Data Resolution

As shown earlier, the thickness of the detected edge is related to template size. However, edge thickness is also related to the resolution of the image. Three different data resolutions were applied. Processing was performed using every other point, every fourth point, and every eighth point of the original field. The coarser data resolution resulted in thicker edges (Figure 32). It should be noted that, in polar coordinates, the physical interval between data points is variable. The data spacing is a constant along the radar beam and with respect to angle. However, the true spatial distance between beams increases with range. This affects the resolution in the gradient computation. The detected edges at longer ranges are not as sharp as those near the radar. Our present computer capacity has limited data processing to every other point. In general, though, better results should be obtained when all data are used in the analyses.

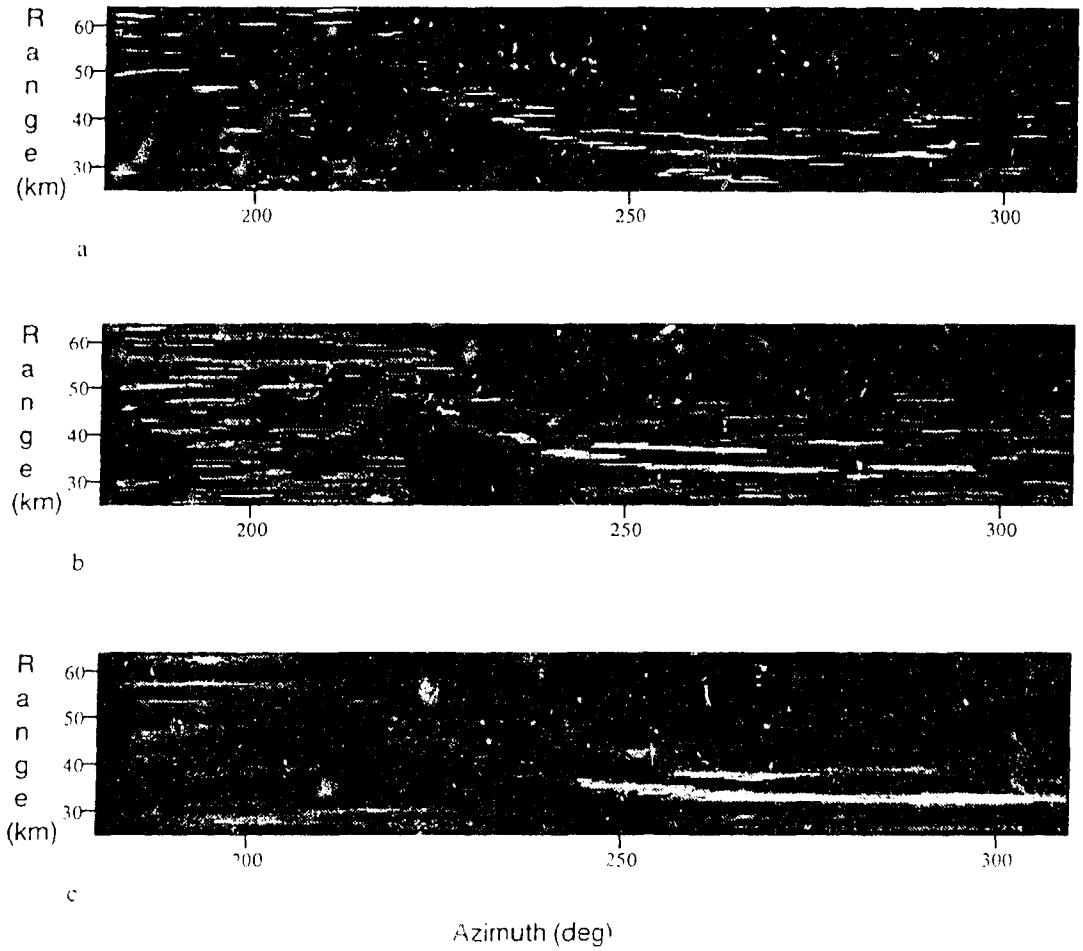

Figure 32 . Edge points for reflectivity field for different data resolutions: (a) every other point, (b) every fourth point, (c) every eighth point.

4.2.3.6.Feature Combining

From the analyses presented above, it should be apparent that frontal extraction can not be adequately accomplished with only one simple technique. Noise, missing data, and orientation effects all tend to present complications to the analyses. It is therefore necessary to mitigate these problems with additional procedures such as thresholding and combining features. Noise produces unexpected features in both the velocity and reflectivity gradient fields. A way to eliminate some of these spurious features is to check for consistency of features between the fields. Locations of features extracted from the velocity gradient

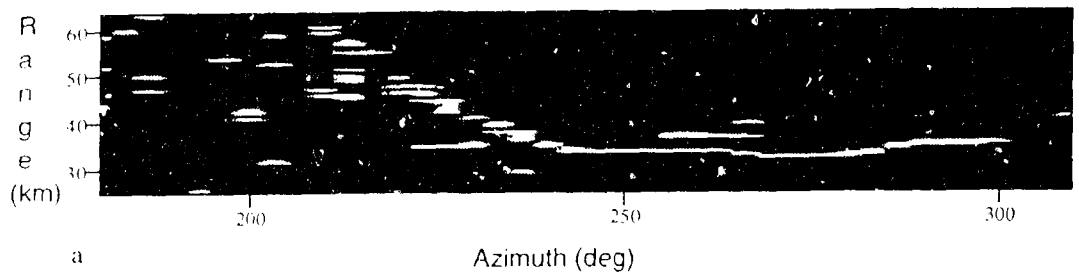

Figure 33. Features in the velocity gradient field.

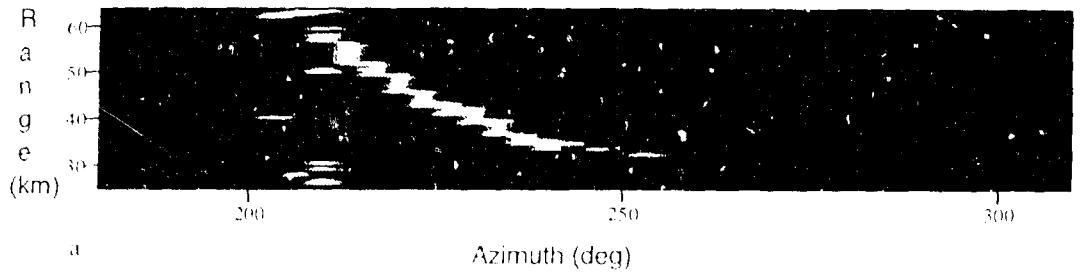

Figure 34. Features in the reflectivity gradient field.

vectors, the reflectivity gradient vectors, and the enhanced reflectivity zone in the reflectivity field are compared. Collocated features from two or more fields are retained. Figure 33 depicts the feature extracted from the velocity gradient field. The gradient boundary is more or less aligned along the frontal position. Figure 34 depicts the feature extracted from the reflectivity gradient field. There are two gradient boundaries along the outer edges of the maximum reflectivity band. Gradients are small within the narrow band. No distinguishable features appear at azimuths greater than 250

Figure 35 depicts the maximum reflectivity band along the thin line extracted from the reflectivity field. In general, a thin line is a long thin zone of enhanced reflectivity. The thin line appearing in the reflectivity field is associated with the line convection of the cold front. While the reflectivity gradients are utilized in the feature identification process, the maximum reflectivity band along the thin line provides a more definite boundary.

Fuzzy logic (.AND. or .OR.) is applied to combine features extracted from the radial velocity gradient, reflectivity gradient, and reflectivity magnitude. The .AND.

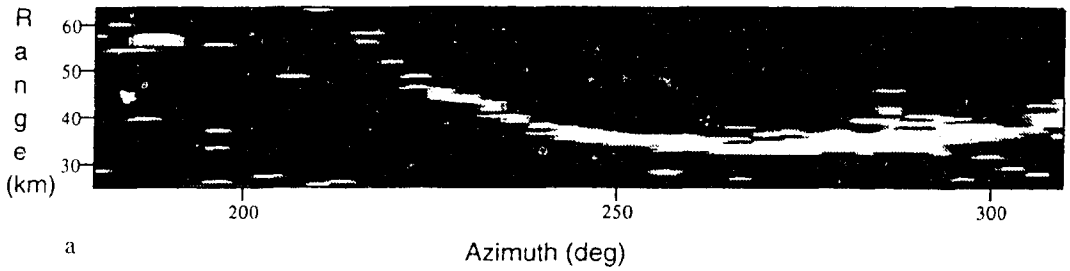

Figure 35. Enhanced reflectivity zone

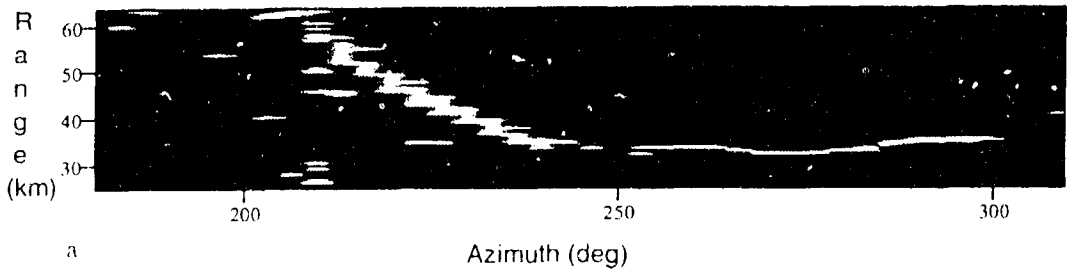

Figure 36 . Combined front feature.

logic is applied to extract only the edges that satisfied the detection thresholds for the gradient magnitude and direction. Combinations of the velocity gradient vector fields, the reflectivity gradient vector fields, and the enhanced reflectivity field are utilized. A unit index is assigned to each edge for each field. The .OR. logic is applied to gather all the possible edges from all files. That means a weight for each edge is computed by summing up indices. A thresholding technique is then applied to discriminate against undesirable features. Figure 36 depicts the combined front feature. A frontal feature is identified as a single continuous boundary aligned with the front position.

4.3. Summary

In this report, a frontal detection algorithm using a gradient technique based in polar coordinates is presented. The algorithm has been applied to a cold front case. Alternative noise filters have been tested and compared. The algorithm has been tested for various operator sizes and structures, gradient magnitude computations, data resolutions, and feature extraction procedures.

All the computations and implementations were performed on a personal computer with limited storage and memory. Only a portion of the front can be processed with each run. The data resolution was limited to every other point.

Although the algorithm provides promising results, there are still difficulties in automation of the processes used in computer vision. Humans have a talent for dealing with uncertain, ambiguous, and even contradictory evidence. The machine intelligence is more limited. More sophisticated and more advanced tools have the potential of providing a great diversity of methods for improving the algorithm development.

The technique developed under this task not only provides a tool for the focusing of further frontal analysis, but it also provides the basis for the extraction of quantitative frontal information. The structure of the reflectivity and the radial velocity fields and their gradient fields are expected to provide indications of the

magnitude and behavior of associated hazards. Efforts during the upcoming year will focus on the utilization of these fields in the characterization of the three-dimensional frontal structure.

5. DEVIATIONS FROM RESEARCH PLAN

One event and one non-event had negative impacts on the performance on this contract. The event was the move of government and Hughes STX personnel from the Radar Facility in Sudbury to Hanscom AFB. Because there were so few government personnel and there was so much stuff to deal with, the accumulation of scores of people over 30 years, Hughes STX personnel had to assist in the move. This meant that there was one month (August) that was solidly devoted to the move and another half month of impact involved in settling in at the new facility. The non-event has been the delay introduced by the government procurement process in the acquisition of new processing/display equipment. To perform the tasks under this contract it is essential that we are able to access and process data collected by the NEXRAD radar systems. This is not possible with the equipment currently available for this project. The necessary equipment has been ordered by the government and receipt is expected within the next few months.

The result of these two situations is that progress has not been as fast or as dramatic as anticipated. We have met our goals but not with the level of product that we had hoped. We anticipate that we will be able to make up any lost ground in this next year.

6. PLANS FOR NEXT CONTRACT YEAR

6.1. Severe Storm Structure

During the next year of the contract, efforts on this task will be directed toward the further development of techniques for the detection and quantization of the

BWER. These techniques will be implemented on the new workstations and will initiate evaluation with NEXRAD data.

6.2. Lightning Prediction in Air Mass Thunderstorms

For lightning detection, techniques will be drawn from the other two tasks and integrated into a lightning precursor technique. Evaluation of these techniques will begin using data from NEXRAD and the lightning network.

6.3. Frontal Structure

In the second year of this contract, the front detection algorithm will be transferred to a Unix - based workstation and adapted to depict the three - dimensional wind field and reflectivity structure associated with the front.

7. REFERENCES

Achtemeier, G.L., 1991: The use of insects as tracers for "clear-air" boundary-layer studies by Doppler radar. J.Tech.Atmos. Oceanic Technol.. 8, 746-765.

Armstrong, G. M., and R. D. Donaldson, Jr., 1969: Plan Shear Indicator for Real-Time Doppler Radar Identification of Hazardous Storm Winds. *J. Appl. Meteor.*, **8**, 376-383.

Ballard, D.H. 1981: Generalizing the Hough Transform to detect arbitrary shapes. Pattern Recognition, 13, 111.

Bluestein, H. B., and C. R. Parks, 1983: A Synoptic and Photographic Climatology of Low-Precipitation Severe Thunderstorms in the Southern Plains. *Mon. Wea. Rev.*, **111**, 2034-2046.

Bluestein, H. B., and G. R. Woodall, 1990: Doppler-Radar Analysis of a Low-Precipitation Severe Storm. *Mon. Wea. Rev.*, **118**, 1640-1664.

Breed, D.W., 1993: Electric field development and multi-parameter radar measurements in a Florida storm. Preprints, 17th Conf. on Severe Local Storms and Conference on Atoms. Elect., St. Louis, American Meteorological Soc., Boston, MA, J16-J19.

Bringi, V.N., A. Detwiler, V. Chandrasekar, P.L. Smith, L. Lieu, I.J. Caylor and D. Musil, 1993: Multiparameter radar and aircraft study of the transition from early to mature storm during CaPE: the case of 9 August 1991. Preprints, 26th Conf. on Radar Meteor., Norman, OK, Amer. Meteor. Soc., Boston, MA, 318-320.

Bringi, V.N., I.J. Caylor, J. Turk, and L. Lin, 1993: Microphysical and electrical evolution of a convective storm using multiparameter radar and aircraft data during CaPE. Preprints, 26th Conf. on Radar Meteor., Norman, OK, Amer. Meteor. Soc., Boston, MA, 312-314.

Brooks, H. E., and R. B. Wilhelmson, 1993: Hodograph Curvature and Updraft Intensity in Numerically Modeled Supercells. *J. Atmo. Sci.*, **50**, 1824-1833.

Brown, R. A., 1990: Characteristics of supercell hodographs. *Preprints, 16th Conference on Severe Local Storms*, Kananaskis Park, Canada, Amer. Meteor. Soc., 30-33.

Brown, R. A., 1992: Initiation and Evolution of Updraft Rotation within an Incipient Supercell Thunderstorm. *J. Atmos. Sci.*, **49**, 1997-2014.

Brown, R. A., 1993: A Compositing Approach for Preserving Significant Features in Atmospheric Profiles. *Mon. Wea. Rev.*, **121**, 874-880.

Browning, K. A., and F. H. Ludlam, 1962: Airflow in Convective Storms. *Quart. J. R. Meteor. Soc.*, **88**, 75-84.

Browning, K. A., and R. J. Donaldson, Jr., 1963: Airflow and Structure of a Tornadic Storm. *J. Atmos. Sci.*, **20**, 533-545.

Buechler, D.E. and S.J. Goodman, 1991: Radar characteristics of cloud-to-ground lightning producing storms in Florida. Preprints, 25th Conf. on Radar Meteor., Paris, France, Amer. Meteor. Soc., Boston, MA, 897-900.

Buechler, D.E., P.D. Wright, and S.J. Goodman, 1990: Lightning/rainfall relationships during COHMEX. Preprints, 16th Conf. on Severe Local Storms., Kananaskis Park. Amer. Meteor. Soc., Boston, MA, 710-714.

Burgess, D W., and L. R. Lemon, 1990: Severe Thunderstorm Detection by Radar. Radar in Meteorology, Atlas, D., ed., Amer. Meteor. Soc., Boston, MA, 619-647.

Burgess, D. W., R. J. Donaldson, T. Sieland, and J. Hinkelman, 1979: Final report on the Joint Doppler Operational Project (JDOP) 1976-1978. Part I - Meteorological applications. NOAA Technical Memorandum ERL NSSL-86. U. S. Dept. of Commerce. 84 pp.

Byers, H. R., and R. R. Braham, Jr., 1949: *The Thunderstorm*. Supt. of Documents, U. S. Government Printing Office, Washington, D. C., 287 pp.

Chisholm, A. J., 1973: Alberta Hailstorms Part I: Radar Case Studies and Airflow Models. *Meteor. Monogr.*, **14**, Amer. Meteor. Soc., Boston, 1-36.

Delanoy, R. L. and S. W. Troxel, 1993: Machine Intelligent Gust Front Detection. *Linc. Lab. J.*, **6**, 187-212.

Detwiler, A.G., J.H. Helsdon, D.J. Musil, R. Ramachandran, P.L. Smith, V.N. Bringi, and I.J. Caylor, 1993: Observations of electrification in CaPE thunderstorms. Preprints, 17th Conf. on Severe Local Storms, St. Louis, MO, Amer. Meteor. Soc., Boston, MA, J8 - J15.

Donaldson, Jr., R. D., 1970: Vortex Signature Recognition by a Doppler Radar. *J. Appl. Meteor.*, **9**, 661-670.

Donaldson, Jr., R. J., 1961: Radar Reflectivity Profiles in Thunderstorms. *J. Meteor.*, **18**, 292-305.

Donaldson, Jr., R. J., 1962: Radar Observations of a Tornado Thunderstorm in Vertical Section. NSSP Report No. 8, U. S. Weather Bureau, 1-21.

Donaldson, Jr., R. J., 1990: Foundations of Severe Storm Detection by Radar. Radar in Meteorology, Atlas, D., ed., Amer. Meteor. Soc., Boston, MA, 115-121.

Donaldson, Jr., R. J., A. C. Chmela and C. R. Shackford, 1960: Some Behavior Patterns of New England Hailstorms. Monogr. No. 5, American Geophysical Union, 354-368.

Donaldson, R.J., Jr. and D.W. Burgess, 1982: Results of the Joint Doppler Operational Project. Proc. NEXRAD Doppler Radar Symposiom/Workshop, CIMMS, Univ. Ofla, 102-103.

Dye, J.E., W.P. Winn, J.J. Jones, and D.W. Breed, 1989: The electrification of New Mexico thunderstorms. 1. Relationship between precipitation development and the onset of electrification. J. Geophys. Res., 94, 8643 - 8656.

Eilts, M.D., E.D. Mitchell, and K. Hondl, 1991: The use of Doppler radar to help forecast the development of thunderstorms, Preprints, 25th Conf. on Radar Meteor., Paris, France, Amer. Meteor. Soc., Boston, MA, 63-66.

Goodman, S.J., and R. Radhavan, 1993: Investigation the relation between precipitation and lightning using polarimetric radar observations. Preprints, 26th Conf. on Radar Meteor., Norman, OK, Amer. Meteor. Soc., Boston, MA, 793 - 795.

Goodman, S.J., D. E. Buechler, PID. Wright, W.D. Rust, and K.E. Nielson, 1989: Polarization radar and electrical observations of microburst producing storms during COHMEX. Preprints, 24th Conf. on Radar Meteor., Tallahassee, Amer. Meteor. Soc., Boston, MA, 109-112.

Hamann, D.J., 1991: Front detection with Doppler radar. STX Scientific Report, #3, PL-TR-91-2034, ADA242880.

Herzgh, P.H., and A.R. Jameson, 1992: Observing precipitation through dual-polarization radar measurements. Bull. Amer. Meteor. Soc., 73, 1376-1374.

Hubel, D.H. and T.N. Wiesel, 1979: Brain mechanisms of vision. Scientific American, Sept. 150-162.

Illingworth, A.J., J.W.F. Goddard, and S.M. Cherry, 1987: Polarization radar studies of precipitation development in convective storms. Quart J. Roy. Meteor. Soc., 113, 469-489.

Juvanon du Vachat, R., and J.-L. Cheze, 1993: The ASPIC project: presentation of a short-range forecasting system for storms and precipitations, [and] preliminary evaluation of the SAFIR lightning system. Preprints, 17th Conf. on Severe Local Storms, St. Louis, MO, Amer. Meteor. Soc., Boston, MA, 756 - 760.

Keenan, T., R. Potts, and T. Stevenson, 1992: An evaluation of the Darwin area forecast experiment storm occurrence forecasts. Wea. Forecasting, 7, 515-523.

Klazura, G. E., and D. A. Imy, 1993: A Description of the Initial Set of Analysis Products Available from the NEXRAD WSR-88D System. *Bull. Amer. Meteor. Soc.*, **74**, 1293-1311.

Laroche, P., C. Malherbe, A. Bondiou, M. Weber, c. Engholm, and V. Coel, 1991: Lightning activity in microburst producing storm cells. Preprints, 25th Conf. on Radar Meteor., Paris, France, Amer. Meteor. Soc., Boston, MA, J85 - J88.

Lemon, L. R., 1977: New severe thunderstorm radar identification techniques and warning criteria: a preliminary report. NOAA Technical Memorandum NWS NSSFC-1. U. S. Dept. of Commerce, 60 pp.

Lemon, L. R., and C. A. Doswell III, 1979: Severe Thunderstorm Evolution and Mesocyclone Structure as Related to Tornadogenesis. *Mon. Wea. Rev.*, **107**, 1184-1197.

Lhermitte, R.M., and P. Krehbiel, 1979: Doppler radar and radio observations of thunderstorms. IEEE Trans. on Geoscience Electronics, 17(4), 162-171.

Lopez, R.E., W.D. Otto, J.R. Daugherty, and R.L. Holle, 1989: The relationshoip between radar and lightning characteristics of northeastern Colorado storm systems. Preprints, 24th Conf. on Radar Meteor., Tallahassee, Amer. Meteor. Soc., Boston, MA, 85 - 88.

Mansur, M. V., 1993: Examples of the Strengths and Weaknesses of the WSR-88D Storm Tracking Product. *Preprints, 26th International Conference on Radar Meteorology*, Amer. Meteor. Soc., 144-146.

Mecikalski, J. R., and E. C. Evenson, 1993: A Comparison of Composite Hodographs of the Great Lakes Region and the Western Great Plains. *Preprints, 17th Conference on Severe Local Storms*, St. Louis, MO, Amer. Meteor. Soc., 65-69.

Moller, A. R., C. A. Doswell and R. W. Pryzbylinski, 1990: High-precipitation supercells: A conceptual model and documentation. *Preprints, 16th Conference on Severe Local Storms*, Kananaskis Park, Canada, Amer. Meteor. Soc., 52-57.

Morse, A. R., R. W. Pryzbylinski and R. Czys, 1993: Doppler Radar Observations of a High-Precipitation Supercell Associated with Damaging Winds and Tornadoes. *Preprints, 26th International Conference on Radar Meteorology*, Amer. Meteor. Soc., 202-205.

Nadler, M. and E. P. Smith, 1993: Pattern Recognition Engineering. John Wiley and Sons, Inc., New York, NY, 588 pp.

Nelson, S. P., 1987: The Hybrid Multicell-Supercell Storm- An Efficient Hail Producer. *J. Atmos. Sci.*, **44**, 2060-2073.

Nielsen, K.E., S.J. Goodman, and D.E. Buechelr, 1990: Cloud-to-ground lightning and rainfall volumes in mesoscale convective systems. Preprints, 16th Conf. on Severe Local Storms., Kananaskis Park, Amer. Meteor. Soc., Boston, MA, 634 - 638.

Petersen, W.A., S.A. Rutledge, D.J. Boccippio, and E.R. Williams, 1993: The electrification of tropical oceanic convective clouds observed during TOGA-COARE. Preprints, 17th Conf. on Severe Local Storms, St. Louis, MO, Amer. Meteor. Soc., Boston, MA, 796-802.

Pryzbylinski, R. W., T. D. Shea, D. L. Ferry, E. H. Goetsch, R. R. Czys, and N. E. Westcott, 1993: Doppler Radar Observations of High-Precipitation Supercells Over the Mid-Mississippi Valley Region. *Preprints, 17th Conference on Severe Local Storms*, St. Louis, MO, Amer. Meteor. Soc., 158-163.

Purdom, J.F.W., 1973: Satellite imagery and the mesoscale convective forecast problem. Preprints, 8th Conf. on Severe Local Storms, Denver, CO, Amer. Meteor. Soc., Boston, MA, 244 - 2521.

Ray, P., 1990: Convective Dynamics. Radar in Meteorology, Atlas, D., ed., Amer. Meteor. Soc., Boston, MA, 348-390.

Reynolds, S.E., and M.Brook, 1956: Correlation of the initial electric field and the radar echo in thunderstorms. J. Meteor., 13, 376 - 380.

Richard, P. 1990: SAFIR system: an application of real-time VHF lightning localization to thunderstorm monitoring. Preprints, 16th Conf. on Severe Local Storms., Kananaskis Park, Amer. Meteor. Soc., Boston, MA, J21 - J26.

Richard, P., 1991: Localization of atmospheric discharges, a new way for severe weather nowcasting. Preprints, 25th Conf. on Radar Meteor., Paris, France, Amer. Meteor. Soc., Boston, MA, 911 - 915.

Rogers, D., F.W. Wilson, Jr., and R.K. Goodrich, 1991: A feature identification algorithm. Preprints, 25th Conf. on Radar Meteor., Paris, France, Amer. Meteor. Soc., Boston, MA, 115 - 118.

Rotunno, R., 1986: Tornadoes and Tornadogenesis. Mesoscale Meteorology and Forecasting, Ray, P. S., ed., Amer. Meteor. Soc., Boston, MA, 414-436.

Saunders, C.P.R., 1993: A review of thunderstorm electrification processes. J. Appl. Meteor., 32,642 - 655.

Seliga, T.A., K. Aydin, and H. Direskeneli, 1986: Disprometer measurements during an intense rainfall event in central Illinois: implications for differential reflectivity radar observations. J. Climate and Appl. Meteor., 25, 835 - 846.

Shackford, C.r., 1960: Radar indications of a precipitation - lightning relationship in New England thunderstorms. J. Meteor., 17, 15 - 17.

Shchukin, G.G., S.M. Galperin, V.N. Stasenko, V.I. Bannikov, V.I. Frolov, and I.I. Tarabukin, 1993: Complex radiophysical cumulonimbus study. Preprints, 26th Conf. on Radar Meteor., Norman, OK, Amer. Meteor. Soc., Boston, MA, 685 - 686.

Weaver, J. F., and S. P. Nelson, 1982: Multiscale Aspects of Thunderstorm Gust Fronts and Their Effects on Subsequent Storm Development. *Mon. Wea. Rev.*, **110**, 707-718.

Weber, M., R. Boidi, P.Laroche, P. Krehbiel, and X.-M. Shao, 1993: Use of high resolution lightning detection and localization sensors for hazardous aviation weather nowcasting. Preprints, 17th Conf. on Severe Local Storms, St. Louis, MO, Amer. Meteor. Soc., Boston, MA, 739 - 744.

Weisman, M. L., and J. B. Klemp, 1986: Characteristics of Isolated Convective Storms. Mesoscale Meteorology and Forecasting, Ray, P. S., ed., Amer. Meteor. Soc., Boston, MA, 331-358.

Wilson, J.W. and W.E. Schreiber, 1986: Initiation of convective storms at radar-observed boundary-layer convergence lines. Mon. Wea. Rev., 114, 2516-2536.

Wilson, J.W., and C.K. Mueller, 1993: Nowcasts of thunderstorm initiation and evolution. Wea. Forecasting, 8, 113 - 131.

Wilson, J.W., and R.E. Carbone, 1984: Nowcasting with Doppler radar: The forecaster - computer relationship. nowcasting II, K. Browning, Ed., European Space Agency, 177 - 186.

Wilson, J.W., and W.E. Schreiber, 1986: Initiation of convective storms at radar - observed boundary - layer convergence lines. Mon. Wea. Rev., 114, 2516 - 2536.

Wilson, J.W., T.M. Weckworth, and R.M. Wakimoto, 1993: Boundary layer radar echoes: origin and applications. Preprints, 26th Conf. on Radar Meteor., Norman, OK, Amer. Meteor. Soc., Boston, MA, 484 - 486.

Witt, A., and J. T. Johnson, 1993: An Enhanced Storm Cell Identification and Tracking Algorithm. *Preprints, 26th International Conference on Radar Meteorology*, Amer. Meteor. Soc., 141-143.